# Subgap states spectroscopy in a quantum dot coupled to gapped hosts: Unified picture for superconductor and semiconductor bands

Peter Zalom [1,*] and Martin Žonda [2,†]

[1]*Institute of Physics, Czech Academy of Sciences, Na Slovance 2, CZ-18221 Praha 8, Czech Republic*
[2]*Department of Condensed Matter Physics, Faculty of Mathematics and Physics, Charles University, Ke Karlovu 5, CZ-12116 Praha 2, Czech Republic*

We present a unified theory of quantum phase transitions for half-filled quantum dots (QDs) coupled to gapped host bands. We augment the bands by an additional weakly coupled metallic lead, which allows us to analyze the system by using standard numerical renormalization-group techniques. The ground-state properties of the systems without the additional metallic lead are then extrapolated in a controlled way from the broadened subgap spectral functions. We show that a broad class of narrow-gap-semiconductor tunneling densities of states (TDOSs) support the existence of two distinct phases known from their superconducting counterpart: the 0 phase, which is marked by the singlet ground state, and the $\pi$ phase regime with the doublet ground state. To keep a close analogy with the superconducting case, we focus on the influence of particle-hole asymmetry of the TDOS on the subgap spectral features. Nevertheless, we also discuss the possibility of inducing singlet-doublet quantum phase transitions in experimental setups by varying the filling of the QD. In addition, for gapped TDOS functions with smoothed gap edges, we demonstrate that all subgap peaks may leak out of the gap into the continuous part of the spectrum, an effect that has no counterpart in the superconducting Anderson model.

## I. INTRODUCTION

Low-temperature nanostructures, e.g., single molecules or various types of semiconducting quantum dots (QDs) coupled to a large system, represent a highly controllable testbed for various concepts of heavy fermion physics. For example, by using metallic host bands one can recreate the Kondo effect [1–6], while opening a superconducting gap $\Delta$ induces 0-$\pi$ quantum phase transitions (QPTs) with two phases of different ground-state parities [7–23].

Microscopic theories for impurities in host bands often rely on the prolific Anderson impurity model (AIM) [24], originally introduced for metallic hosts. For the superconducting case, a BCS mean-field theory is employed and the resulting model is known as the superconducting AIM (SC-AIM). Although the Kondo screening can be suppressed by the spectral gap, the SC-AIM has a similarly complicated hierarchy of coupled energy scales to that of the AIM, which represents a major obstacle for its exact solutions. Analytically, nonperturbative renormalization group (RG) [25–27] or effective renormalization techniques [28–31] are able to capture qualitative behavior, while numerically, quantum Monte Carlo (QMC) techniques provide the most flexible methods but are limited to finite temperatures [32,33]. In contrast, applying RG transformation numerically, i.e., via numerical renormalization group (NRG), offers unbiased access to wide parameter ranges [5,6,13,15,17,34–43].

A significant amount of experimental and theoretical progress has been achieved for various setups of metallic and superconducting leads. However, gapped hosts without pairing correlations, e.g., narrow-gap semiconductors, have attracted much less attention. For half-filled QDs, there is a growing consensus that a particle-hole (*ph*) symmetric gapped host allows only a doublet ground state, while away from half-filling of the QD a critical size of spectral gap $\Delta_c$ exists below which a singlet is formed. These results have been established perturbatively [44,45] as well as nonperturbatively by QMC [46] and NRG [47–49]. However, the logarithmic discretization of the band, upon which NRG relies, fails [47–49] for energies within the finite spectral gap $\Delta$, and nonstandard approaches beyond such limitations have been employed.

Given different physical origins of the semiconducting and superconducting spectral gaps, a direct analogy between the AIM with a semiconductor host and SC-AIM seemed to be unlikely. Nevertheless, in Ref. [50] a half-filled (HF) SC-AIM has been exactly mapped onto a QD coupled to a scalar semiconducting band of Bogoliubov quasiparticle (bogoliubon). The tunneling density of states (TDOS) of this band at the phase-bias $\varphi = \pi$ exactly matches the electronic TDOS of a QD coupled to the armchair graphene nanoribbon (AGNR) with a semiconductor gap [51].

In addition, for SC-AIM the phase-bias $\varphi \neq \pi$ introduces a *ph*-asymmetry into the band of Bogoliubons, which can drive 0-$\pi$ QPTs in the system. The same behavior can then be reproduced with the AGNR host by introducing *ph*-asymmetric TDOS functions that match those of SC-AIM for Bogoliubons [52]. These singlet-doublet QPTs are of an electronic nature, but they still might rely on specific TDOS features that involve

*zalomp@fzu.cz
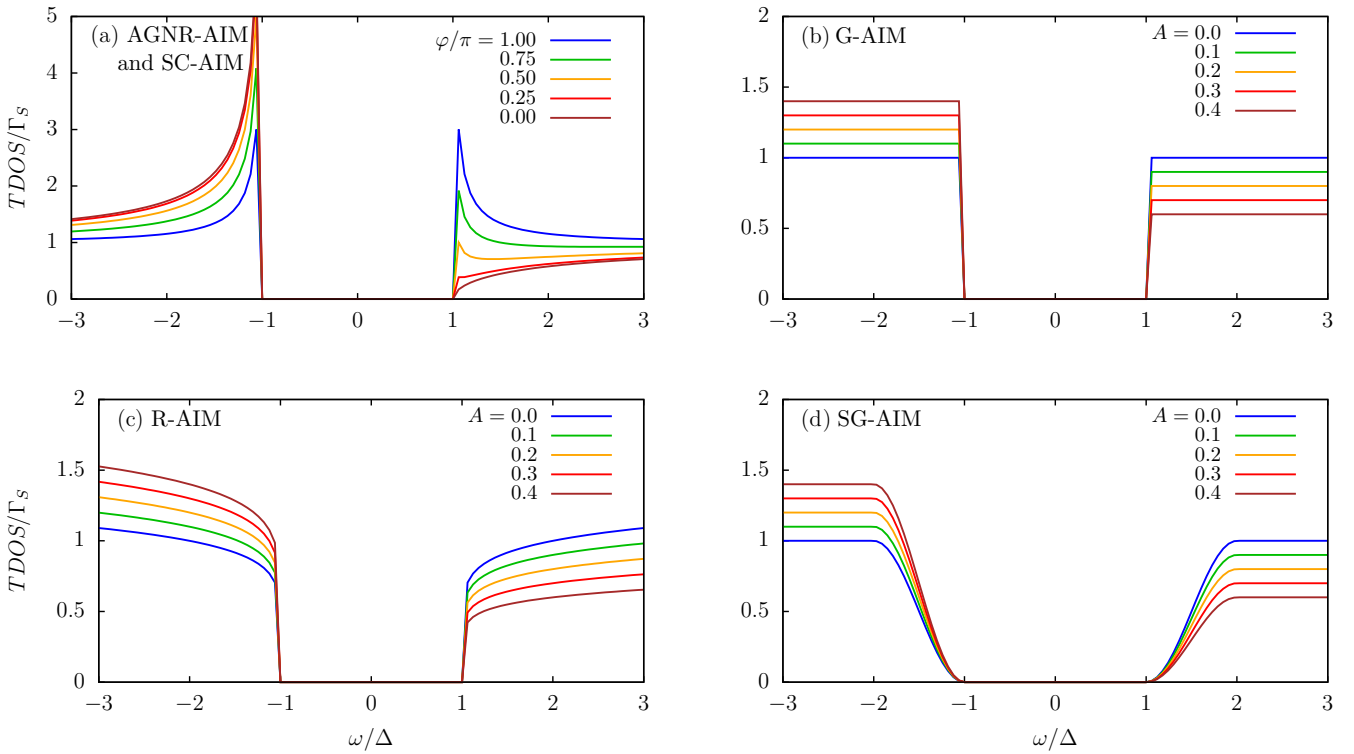†martin.zonda@karlov.mff.cuni.cz

FIG. 1. (a)–(d) TDOS functions of four distinct semiconductor models with various properties. BCS-like divergences on the gap edges appear in (a) and are typical for SC-AIM and AGNR-AIM cases given in Eq. (10). The gapped Anderson model (G-AIM) possesses only finite discontinuities on the gap edges as shown in (b), and it is given in Eq. (12). Continuous TDOS functions appear when root functions are considered (R-AIM case) as given in Eq. (14), and they are shown in (c). Smoothed-out gap edges of the gapped Anderson model are considered in Eq. (13) and are shown in (d). In SC-AIM and AGNR-AIM, $ph$-asymmetry is incorporated via parameter $\varphi$ that modulates the TDOS in the vicinity of the gap edges. In the remaining models, $ph$-asymmetry is incorporated via the parameter $A$.

BCS-like divergences; see Fig. 1(a). It is thus unclear how crucial such specific properties are to allow the existence of QPTs in QDs with semiconductor hosts. To resolve this question, we investigate several classes of semiconductor TDOS functions. These are chosen to represent some typical physical scenarios, e.g., hosts of different dimensionality, and simultaneously they allow us to probe the influence of the spectral gap shape on the QPTs.

In addition to AGNR, we consider a finite steplike discontinuity, representing the DOS of a trivial two-dimensional semiconductor [blue line in Fig. 1(b)]. This type of DOS was addressed before in the studies of the gapped AIM (G-AIM) [47–49], nevertheless only $ph$-symmetric TDOSs have been analyzed. Yet, the $ph$-asymmetry can be significant in real materials. Therefore, we define the parameter $A$ to measure the weight difference between the electronic and hole components of TDOS as shown in Fig. 1. Motivated by the noninteracting cases, where bound states appear only when a critical depth or width of the gap is present [53], we additionally construct continuous TDOS functions. For R-AIM, a root behavior on the gap edges, like the one expected for a three-dimensional host, is considered [Fig. 1(c)]. SG-AIM is constructed from G-AIM by smoothing its discontinuity. Once again, $ph$-asymmetry is incorporated via $A$ analogously to G-AIM.

To circumvent the difficulties arising from truncation strategies for systems with gapped TDOS [47–49], we add metallic leads with constant broadening $\Gamma_M$ to the models,

which are then indicated as SC-AIM+M, AGNR-AIM+M, G-AIM+M, S-AIM+M, and R-AIM+M, respectively. Standard NRG techniques may then be applied [50–52], since the TDOS becomes nonzero in the gap. This comes at the expense of inducing a singlet ground state, which obscures a possible doublet state and related singlet-doublet QPTs expected at $\Gamma_M = 0$.

Nevertheless, by lowering $\Gamma_M$ to the smallest possible value guaranteeing numerical stability of NRG, we can still obtain spectral functions and perform subgap spectroscopy of broadened in-gap features [50–52]. In analogy to the QPTs in SC-AIM, which can be driven by phase-bias induced $ph$-asymmetry of $w$ Bogoliubons, we investigate the evolution of the in-gap features by varying $A$ in semiconductor hosts. In particular, we focus on crossings of the in-gap features with the Fermi energy, which signals an underlying singlet-doublet QPT for $\Gamma_M \to 0$.

The outline of this paper is as follows. We first review the subgap spectroscopy of SC-AIM+M in Sec. II A and AGNR-AIM+M in Sec. II B. In Sec. II C, three other classes of semiconductor TDOS function are defined. An approximative atomic limit theory is formulated in Sec. II D. Temperature-dependent effective models of G-AIM are discussed in Sec. III A, with remaining cases analyzed in Sec. III B. The nature of the underlying QPTs is analyzed for G-AIM in Sec. IV A. In Sec. IV B we confirm that singlet-doublet transitions can be supported by all TDOS functions considered

here. Finally, we argue in Sec. V that a possible experimental realization of a singlet-doublet transition with semiconductor host bands might be simpler with electrostatic gating of the QD. The main conclusions are then summarized in Sec. VI. Some technical aspects are postponed to Appendixes. Namely, the details of the NRG method and resulting RG flows are given in Appendixes A 1–A 4, and the escape of in-gap peaks into the continuum is discussed in Appendix A 5.

## II. THEORY

### A. QPTs in SC-AIM

A single-level QD (impurity) coupled to superconducting host bands can be modeled by the SC-AIM [3,16–18,23] where the impurity is treated as a spin-1/2 Anderson orbital populated by the electrons $d_\sigma$ of spin projections $\sigma \in \{\uparrow, \downarrow\}$. The corresponding Hamiltonian reads

$$H_{\text{dot}} = \sum_\sigma \varepsilon_{\text{dot}} d_\sigma^\dagger d_\sigma + U d_\uparrow^\dagger d_\uparrow d_\downarrow^\dagger d_\downarrow, \qquad (1)$$

where $d_\sigma^\dagger$ creates an electron of spin $\sigma$ on the QD while $d_\sigma$ annihilates it. The first term describes the energy level $\varepsilon_{\text{dot}}$ and the second one the local Coulomb repulsion characterized by $U$. The half-filled point of the QD is therefore set by $\delta = 0$, where $\delta = \varepsilon_{\text{dot}} + U/2$.

The interaction of a QD with BCS and/or metallic lead(s) can analogously be expressed via the corresponding Hamiltonians. Alternatively, as preferred here, one can employ the Nambu spinor $D^\dagger = (d_\uparrow^\dagger, d_\downarrow)$ and integrate out all of the remaining degrees of freedom, which then enter the corresponding Nambu Green's function of $D^\dagger$ only via the tunneling self-energy

$$\Sigma^D(\omega^+) = \Sigma_n^D(\omega^+)\mathbb{1} + \Sigma_a^D(\omega^+)\sigma_x, \qquad (2)$$

whose imaginary part is the corresponding TDOS. Here, $\mathbb{1}$ is a two-by-two unit matrix, $\sigma_x$ is the Pauli matrix $x$, and the self-energy components read

$$\Sigma_n^D(\omega^+) = -i\Gamma_M + \Gamma_S \omega F(\omega^+), \qquad (3)$$

$$\Sigma_a^D(\omega^+) = \Gamma_S \Delta \cos\left(\frac{\varphi}{2}\right) F(\omega^+), \qquad (4)$$

where $\Delta$ is the superconducting gap, $\Gamma_S = \Gamma_L + \Gamma_R$, and $\varphi$ is the phase drop across the BCS leads with the gauge set so that the left BCS lead phase is $\varphi_L = \varphi/2$ while the right one is $-\varphi_R = -\varphi/2$. The function $F(\omega^+)$ reads

$$F(\omega^+) = \begin{cases} -\frac{2}{\pi\sqrt{\Delta^2 - \omega^2}} \arctan\left(\frac{B}{\sqrt{\Delta^2 - \omega^2}}\right) & \text{for } |\omega| < \Delta, \\ -\frac{i\,\text{sgn}(\omega)}{\sqrt{\omega^2 - \Delta^2}} + \frac{\ln\left(\frac{B + \sqrt{\omega^2 - \Delta^2}}{B - \sqrt{\omega^2 - \Delta^2}}\right)}{\pi\sqrt{\omega^2 - \Delta^2}} & \text{for } \Delta < |\omega| < B, \end{cases} \qquad (5)$$

where $2B$ is the width of the host band. For $\Gamma_M = 0$, the model is known as SC-AIM and can be treated by standard superconducting NRG [12,54]. The $\Gamma_M \neq 0$ case is referred to here as SC-AIM+M; for a detailed analysis, see Ref. [50].

Examples of the evolution of normal spectral functions $\mathcal{A}(\omega)$ on $\Gamma_M$ are shown in Figs. 2(a) and 2(c). In the 0-like

regime [Fig. 2(a)], $\mathcal{A}$ exhibits a single pair of broadened ABS peaks at $\omega = \pm E_{\text{ABS}} \approx 0.2\Delta$ but no Kondo-like features. On the contrary, in the $\pi$-like regime [Fig. 2(c)], two pairs of broadened ABS peaks are accompanied by a zero-frequency Kondo-like feature. The $\varphi$-evolution of the maxima of all subgap features is shown in Fig. 2(e) for $\Gamma_M/\Delta = 0.01$. Solid blue lines mark the center position of the broadened ABS peaks, while the dashed blue line traces the center of the Kondo-like resonance.

Note that all normal spectral functions are presented here as normalized according to the Friedel sum rule. Therefore, as $\Gamma_M \to 0$, the broadened ABS peaks quickly lose height when compared to the Kondo-like feature, allowing thus their precise distinction. The spectral weight $\mathcal{W}$ of the ABS peaks, however, remains finite with decreasing $\Gamma_M$ as illustrated in Fig. 2(g). While the weights are relatively stable within the 0- and $\pi$-phase, they exhibit a rather sharp decrease at $\varphi \approx \pi/2$ where the ABS peaks cross the Fermi energy, but the determination of $\mathcal{W}$ becomes complicated in this regime as the ABS peaks merge with the Kondo-like feature. So inferring upon the nature of the subgap features is more reliable from their $\Gamma_M$ and/or $\varphi$ dependences.

We emphasize that in addition to the subgap Kondo feature in $\pi$-like regimes, there is also an emergent supragap ($|\omega| > \Delta$) Kondo effect, which is primarily induced by the superconducting lead. It appears upon closer inspection of the supragap portion of the spectral function as its width is proportional to $\Gamma_S/U$ and typically exceeds the spectral gap. At subgap frequencies it is suppressed and the screening instead induces ABS states in the subgap region. With a metallic lead present, a cascade of two reentrant Kondo peaks is thus possible, as discussed at length in Refs. [51,52]. We stress that supragap Kondo resonances appear also for other gapped models studied here. However, unlike the parameter-dependent positions of subgap features, they are not relevant for the investigation of the possible QPTs in the systems.

### B. QPTs in AGNR-AIM

Coupling a QD characterized by Hamiltonian (1) to an AGNR semiconductor band can be modeled using the TDOS,

$$\Gamma_{\text{AGNR+M}}(\omega) = \Gamma_M + \frac{\Gamma_S |\omega| \Theta(\omega^2 - \Delta^2)}{\sqrt{\omega^2 - \Delta^2}}, \qquad (6)$$

with $\Gamma_S$ ($\Gamma_M$) being the hybridization to the QD to the semiconductor (metallic) host and $\Delta$ is the semiconductor gap [51]. Here, the overall number of states is $\approx 2(\Gamma_M + \Gamma_S)B$ in the wide band limit. Such AGNR-AIM+M is in terms of many-body eigenstates equivalent to the SC-AIM+M at $\varphi = \pi$ [50]. This can be shown by rotating the $d_\sigma$ electrons of (1) via a unitary transformation $\mathbb{T}$:

$$w_\uparrow^\dagger = \sqrt{\frac{1}{2}}(-d_\uparrow^\dagger + d_\downarrow), \qquad (7)$$

$$w_\downarrow^\dagger = \sqrt{\frac{1}{2}}(d_\uparrow + d_\downarrow^\dagger). \qquad (8)$$
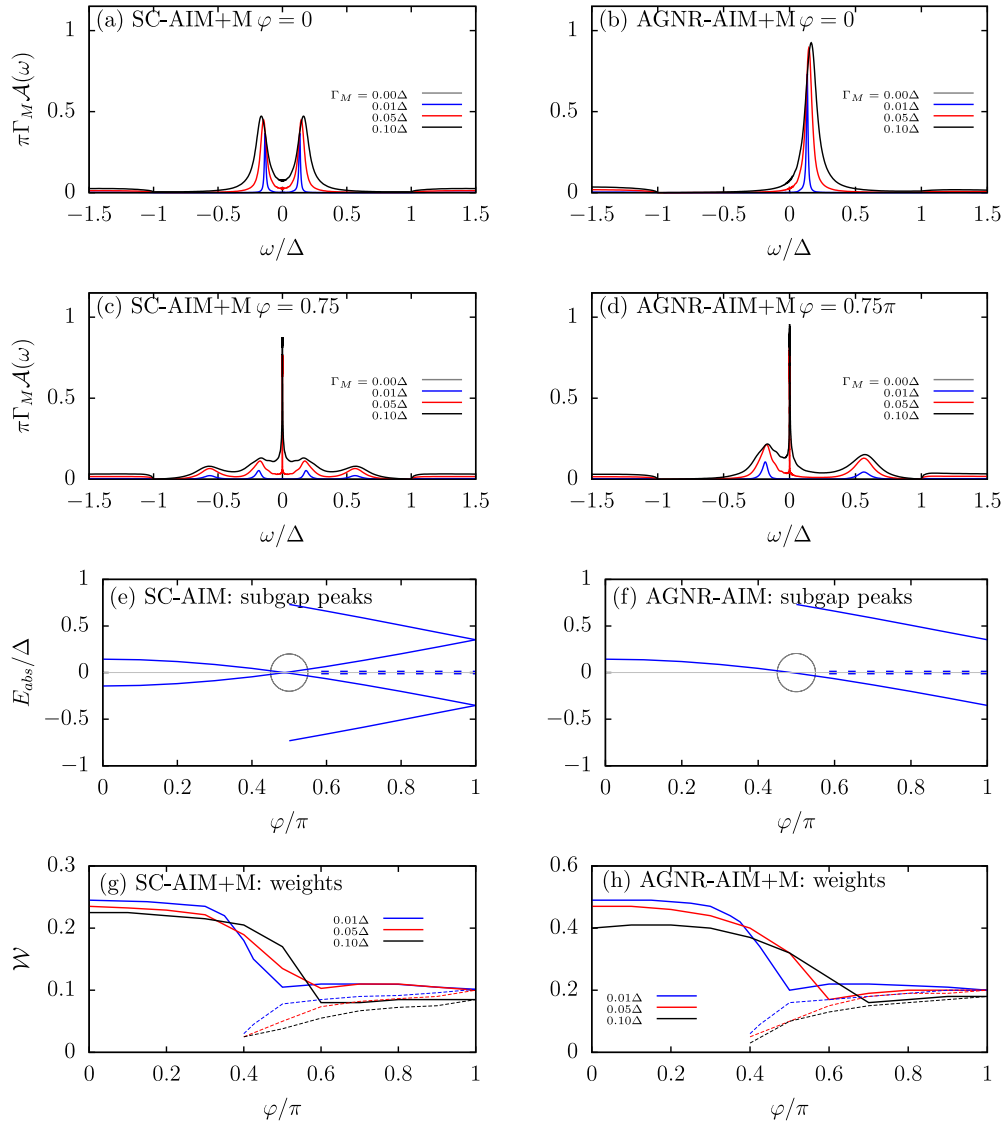
FIG. 2. (a) The normal spectral function $\mathcal{A}(\omega)$ of SC-AIM+M in the 0-like regime ($\varphi = 0$) shows one pair of broadened ABS states. (b) The same as in (a) for AGNR-AIM+M with just one subgap peak at the position matching the right ABS of (a). (c) Increasing $\varphi$ to $0.75\pi$ places the SC-AIM+M into the $\pi$-like regime. Two pairs of symmetrically placed broadened ABS states and a central Kondo peak emerge. (d) The same as in (c) for AGNR-AIM+M. Two asymmetrically placed subgap peaks and one Kondo-like resonance appear. Symmetrizing (b) and (d), the solution for SC-AIM+M in (a) and (c) is obtained. (e),(f) $\varphi$-evolution of subgap peaks. The solid blue line represents the broadened in-gap states, while the dashed line corresponds to the Kondo peak in the $\pi$-like regime. The circle marks the 0-$\pi$ QPT. (g),(h) The spectral weights $\mathcal{W}$ of the in-gap features show a drop around the QPT. The fitting procedure is estimated to have an uncertainty of $\approx 10\%$. Calculations using NRG Ljubljana with discretization parameter $\Lambda = 2$ were performed for $U = 3\Delta$, $\Gamma_S = \Delta$, and $\Delta = 5 \times 10^{-4}B$ with $2B$.

The resulting quasiparticles $w$ are Bogoliubons and allow us to reformulate the QD Hamiltonian to

$$H_{\text{dot}} = \sum_\sigma \varepsilon_{\text{dot}}^w w_\sigma^\dagger w_\sigma + U w_\uparrow^\dagger w_\uparrow w_\downarrow^\dagger w_\downarrow + \delta(w_\uparrow^\dagger w_\downarrow^\dagger + w_\downarrow w_\uparrow),$$
(9)

where $\varepsilon_{\text{dot}}^w = -U/2$ and the last term represents pairing for $w$ quasiparticles, which is proportional to $\delta$ and therefore vanishes in the half-filled dot regime considered here. After the rotation, the corresponding TDOS of $w$ quasiparticles (see Fig. 1) becomes

$$\Gamma_{\text{BCS+M}}^w(\omega; \varphi) = \Gamma_M + \frac{\Gamma_S |\omega| \Theta(\omega^2 - \Delta^2)}{\sqrt{\omega^2 - \Delta^2}} \left(1 - \frac{\Delta}{\omega} \cos\frac{\varphi}{2}\right).$$
(10)

At $\varphi = \pi$, the SC-AIM+M TDOS of $w$ quasiparticles is the same as for AGNR-AIM+M, and consequently both systems have the same many-body spectra. Following Ref. [52], we can then further generalize AGNR-AIM+M and include *ph*-asymmetry as

$$\Gamma_{\text{AGNR-AIM+M}}(\omega; \varphi) \equiv \Gamma_{\text{BCS}}^w(\omega; \varphi),$$
(11)

where $\varphi$ is not a Josephson phase difference as in the case of SC-AIM but rather a measure of electronic band *ph*-asymmetry in AGNR-AIM+M which drives the underlying QPTs at $\Gamma_M = 0$.

The main difference between AGNR-AIM+M and SC-AIM+M appears on the level of one-particle excitations. For

AGNR-AIM+M, the electronic *ph*-asymmetry of the host results in the *ph*-asymmetric spectral functions $\mathcal{A}(\omega)$ with two off-center subgap peaks as shown in Figs. 2(b) and 2(d). These are equivalent to normal spectral functions of rotated SC-AIM+M generated by $w$ quasiparticle excitations. Such spectra can be transformed by symmetrization [see Eq. (34) of Ref. [50]] into standard normal spectral functions of SC-AIM+M so both cases are directly related. Due to the symmetrization, normal spectral functions of SC-AIM+M have always twice as many off-center subgap peaks.

In detail, the electronic *ph*-asymmetry of the AGNR-AIM+M results in *ph*-asymmetric electronic spectral functions $\mathcal{A}(\omega)$. At $\varphi = 0.75\pi$ in Fig. 2(d), the *ph*-asymmetry distorts the central Kondo-like peak, which is slightly shifted from Fermi energy and its height no longer fulfills the Friedel sum rule. The two in-gap peaks emerge in the gap at positions $\omega_+ \approx 0.6\Delta$ and $\omega_- \approx -0.2\Delta$. Increasing further the *ph*-asymmetry, we arrive at $\varphi = 0$ where the former Kondo-like feature disappears due to the *ph*-asymmetry. The in-gap peaks have shifted towards higher frequencies, so that $\omega_+ \rightarrow \Delta$ and its weight decreased beyond possible reliable detection. The in-gap peak formerly at $\omega_-$ then shifted past the Fermi energy up to $\approx 0.2\Delta$. The $\varphi$-dependent position of in-gap features is summarized in Fig. 2(f) and makes clear that the $\varphi$-evolution of SC-AIM+M is in principle its symmetrized version. Consequently, also the spectral weights of in-gap peaks of AGNR-AIM [Fig. 2(h)] contain the combined spectral weight of the in-gap peaks of SC-AIM. This roughly doubles the weights of AGNR-AIM+M in-gap peaks compared to SC-AIM+M.

### C. General semiconducting reservoirs augmented by a normal metallic lead

In general, *ab initio* methods reliably deliver densities of states in the bulk of realistic semiconductor materials [55–57]. However, their interaction with a given nanosystem of interest gives, in principle, realization-dependent TDOS functions [57]. Therefore, instead of investigating specific TDOS functions resembling the bulk properties, we construct

some prototypical TDOS cases where the focus is given to the general features of the *ph*-asymmetry and the shape of the spectral gap. Realistic configurations are discussed briefly in Sec. V.

We first consider TDOS where the BCS-like divergences of AGNR-AIM are replaced by a finite discontinuity as known from the G-AIM [47,48]. We incorporate *ph*-asymmetry of the band via the parameter $A$ as

$$\Gamma_{\text{G-AIM+M}}(\omega) = \begin{cases} \Gamma_M & \text{for } |\omega| < \Delta, \\ \Gamma_M + (1 - \text{sgn}[\omega]A)\Gamma_S & \text{for } |\omega| \geqslant \Delta. \end{cases}$$
(12)

Parameter $A$ thus compares the hole and electronic weights of the TDOS and is bound by $0 \leqslant |A| < 1$ to ensure positive TDOS. $A = 0$ represents the symmetric choice. It is sufficient to restrict the investigation to the positive case $A > 0$ since the negative scenario follows from the symmetry. Note that the integral over all frequencies of the TDOS is fixed to $2\Gamma_M + 2(B - \Delta)\Gamma_S$ for arbitrary $A$. In the wide band limit ($\Delta \ll B$), the integral is $\approx 2(\Gamma_M + \Gamma_S)B$ as for AGNR-AIM+M.

Next, we soften the discontinuity at the gap edge as

$$\Gamma_{\text{SG-AIM+M}}(\omega) = \begin{cases} \Gamma_M & \text{for } |\omega| < \Delta, \\ \Gamma_M + (1 - \text{sgn}[\omega]A)\Gamma_S \times \\ \left[1 - \cos\left(\frac{\pi(|\omega|-\Delta)}{2(b-1)\Delta}\right)\right] \\ \qquad\qquad \text{for } b\Delta \geqslant |\omega| \geqslant \Delta, \\ \Gamma_M + (1 - \text{sgn}[\omega]A)\Gamma_S \\ \qquad\qquad \text{for } |\omega| > b\Delta. \end{cases}$$
(13)

In the resulting SG-AIM+M, $b > 1$ defines the width over which an otherwise finite discontinuity of (12) is smoothed out. Due to the smoothening, some states are removed in the region $\Delta < |\omega| \leqslant b\Delta$, but in the wide band limit with moderate values of $b$ the integral over all frequencies of the TDOS is once again $\approx 2(\Gamma_M + \Gamma_S)B$. We stress that strictly speaking, only the region $|\omega| < \Delta$ exhibits a full gap, however the depletion of the TDOS for $\Delta < |\omega| \leqslant b\Delta$ effectively makes the gap region wider.

So far, the depopulation of TDOS due to the semiconductor gap was limited to the gap-proximity. We therefore construct a continuous TDOS with rootlike behavior at the gap edges as

$$\Gamma_{\text{R-AIM+M}}(\omega) = \begin{cases} \Gamma_M & \text{for } |\omega| < |\Delta|, \\ \Gamma_M + (1 - \text{sgn}[\omega]A)\Gamma_S(|\omega| - \Delta)^{1/r} & \text{for } \omega > \Delta, \end{cases}$$
(14)

where parameter $r > 1$ governs the shape of the TDOS in the whole band. Note that, for a two-dimensional semiconductor, one expects $r \rightarrow \infty$ and the G-AIM model considered previously is recovered, while $r = 2$ would reflect a DOS of a simple three-dimensional bulk system. Moreover, at $A = 0$ TDOS (14) resembles the bulk DOS of granular metallic systems at the onset of the Coulomb blockade regime in two and three dimensions [58,59]. In general, as we discuss in Appendix A 5, small values of $r$ may release the in-gap states into the supragap region. This sets some limits to a possible correspondence between R-AIM and SC-AIM behavior. Therefore, in the following, a typical value of $r$ is set to $r = 8$. In addition, compared to other TDOS functions, the

integral over all frequencies is in the wide band limit given as $2\Gamma_M B + 2r\Gamma_S/(1 + r)$. Therefore, to make quantitative comparisons with other TDOS, we use a scaled $\tilde{\Gamma}_S = (1 + r)\Gamma_S/r$ to match the integral properties.

### D. Atomic limit approximation

While a numerical solution of the models introduced in Secs. II A–II C is possible using NRG, an important insight can be obtained investigating the analytically solvable atomic limit theory [38]. We show later that this interacting, i.e., $U \neq 0$, limit clearly underpins the unified nature of phase transition for systems with various hosts studied in this paper.
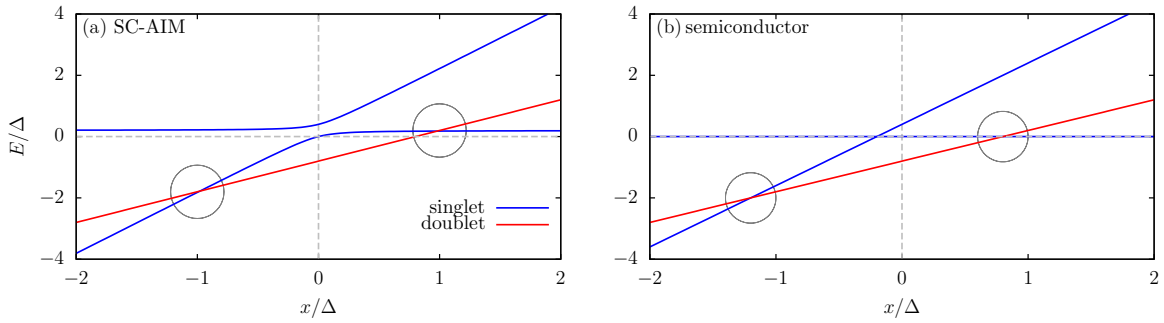
FIG. 3. Panel (a) shows energy eigenvalues in the atomic limit of SC-AIM defined via (16), while in (b) the general semiconductor case (17) is shown. Both panels manifest that the influence of filling of the QD (represented by $\delta$) and the *ph*-asymmetry of the host band (given by $\Gamma_\varphi$ or $\Gamma_A$, respectively) is the same. The symbol $x$ stands for $\delta$ or $\Gamma_\varphi$ and $\Gamma_A$, respectively. In both panels, we set $U = 2\Delta$ while the complementary parameter to $x$ is set to $0.2\Delta$. Note the avoided crossing of singlet energies in SC-AIM and the preserved mirror symmetry in $x$. On the contrary, singlet states of semiconductor host bands cross each other at a point that is shifted away from zero, breaking thus the mirror symmetry in $x$.

For SC-AIM, an effective local Hamiltonian in the atomic limit is known to take the form

$$H_{\text{BCS,d}}^{\text{eff}} = \sum_\sigma \varepsilon_{\text{dot}} d_\sigma^\dagger d_\sigma + U d_\uparrow^\dagger d_\uparrow d_\downarrow^\dagger d_\downarrow - \Gamma_\varphi (d_\uparrow^\dagger d_\downarrow^\dagger + d_\downarrow d_\uparrow),$$

(15)

where $\Gamma_\varphi = (\Gamma_S/\pi) \arctan(B/\Delta) \cos(\varphi/2)$ [38]. This effective model follows from the low-frequency limit of the real part of the tunneling self-energy. Hamiltonian (15) can be solved analytically. Its energy eigenvalues are $\delta \pm \Gamma_\varphi \sqrt{1 + (\delta/\Gamma_\varphi)^2}$ for the singlet states and $\varepsilon_{\text{dot}}$ for the doublet state.

Applying the transformation (8), we obtain the atomic limit in terms of Bogoliubons $w$. It reads

$$H_{\text{BCS,w}}^{\text{eff}} = \sum_\sigma (\varepsilon_{\text{dot}}^w + \Gamma_\varphi) w_\sigma^\dagger w_\sigma + U w_\uparrow^\dagger w_\uparrow w_\downarrow^\dagger w_\downarrow$$
$$+ \delta (w_\uparrow^\dagger w_\downarrow^\dagger + w_\downarrow w_\uparrow) + \delta,$$

(16)

where a constant term $-\Gamma_\varphi$ has been omitted. Note that this term is essential for correct determination of Josephson current via the first derivation of the ground-state energy with respect to $\varphi$ [17], but it does not play a role in the forthcoming analysis. The energy eigenvalues without this term read $(\delta + \Gamma_\varphi) \pm \sqrt{\delta^2 + \Gamma_\varphi^2}$ for the singlet states and $-U/2 + (\delta + \Gamma_\varphi)$ for the doublet state. Thus it is evident that $\delta$ and $\Gamma_\varphi$ exert essentially the same influence on the energy eigenstates.

For AGNR-AIM, G-AIM, SG-AIM, and R-AIM, the atomic limit leads to

$$H_{\text{semi}}^{\text{eff}} = \sum_\sigma (\varepsilon_{\text{dot}} + \Gamma_A) d_\sigma^\dagger d_\sigma + U d_\uparrow^\dagger d_\uparrow d_\downarrow^\dagger d_\downarrow,$$

(17)

where $\Gamma_A$ is a host-specific monotonous function of $A$ that vanishes at $A = 0$ for all *ph*-symmetric host bands. We do not state an explicit functional dependencies of $\Gamma_A$ for each semiconductor model discussed here as for all our purposes we can simply treat it as a model parameter. The eigenstates of the atomic limit model (17) consist of two singlets with energies $(\delta + \Gamma_A) \pm (\delta + \Gamma_A)$, and one doublet with energy $-\frac{U}{2} + (\delta + \Gamma_A)$.

The energy eigenvalues of (16) and (17) depend thus analogously upon $\delta$ and $\Gamma_\varphi$ or $\Gamma_A$, respectively. At half-filling

($\delta = 0$), both models lead to identical expressions no matter the details of the host TDOS. Then, $\Gamma_\varphi$ and $\Gamma_A$ fulfill identical roles. Introducing a finite value of $\delta$ or $\Gamma_\varphi$ ($\Gamma_A$) and varying the other parameter, as shown in Fig. 3, reveals some important differences between both cases. Denoting by $x$ the fixed parameter, the singlets clearly avoid crossing in the superconducting case and an overall left-right symmetry around $x = 0$ is present. In contrast, for semiconductor hosts, the singlets do not avoid crossings and the left-right symmetry around $x = 0$ is broken. Nevertheless, in both cases the doublet energy is the same. As a result, two singlet-doublet QPTs occur as marked by circles in Fig. 3.

Consequently, in the atomic limit we observe that the host band *ph*-asymmetry plays exactly the same role as the *ph*-asymmetry of the QD. In the superconductor case, the sign of the *ph*-asymmetries does not play a role. On the contrary, in the semiconductor host one of the singlet-doublet crossings, i.e., the right one in Fig. 3, is independent of $\delta$ or $\Gamma_A$ while the other may be correspondingly shifted to any desired position by either $\delta$ or $\Gamma_A$. Thus, while Fig. 3 shows an analogous behavior for both models, semiconductors have an additional regime at very large negative values of $\delta$ or $\Gamma_A$, where the singlet becomes always the ground state of the system at arbitrary choices of the remaining model parameters. In such regimes, no QPTs would be observed at all.

The atomic limit approximation thus clearly shows a unified nature of both problems at $\delta = 0$ or $\Gamma_\varphi = \Gamma_A = 0$ while differences arise only at very large negative values of $\delta$ or $\Gamma_A$ which are attributed to the missing avoided crossing of the singlets in the semiconductor case.

## III. TEMPERATURE-DEPENDENT EFFECTIVE MODELS AND THERMODYNAMIC PROPERTIES

### A. Reentrant effective behavior of G-AIM

In addition to the unbiased treatment of interactions, a huge advantage of NRG lies in a rigorous identification of effective impurity models at different energy scales by obtaining the RG flows of eigenenergies, which constitute the basic tool of NRG. As an introduction to this method, the seminal papers by Wilson *et al.* [34–36] as well as the more recent review of NRG for impurity problems [37] can be used.

For convenience, we review the most relevant results for the *ph*-asymmetric AIM and its fixed points in Appendix A 2. The reason is that qualitatively the same flow dependence appears also for the *ph*-asymmetric semiconductor hosts investigated herein. The five relevant fixed points, appearing in both systems, correspond to effective models and are known as the free orbital (FO), valence fluctuation (VF), local moment (LO), frozen impurity (FI), and strongly coupled (SC) fixed point. Their emergence for G-AIM at $A = 0$ is explained in detail in Appendix A 3 and for $A \neq 0$ in Appendix A 4.

Two main results follow from such a detailed analysis. First, at arbitrary $A$ we observe a sequence of two RG flows: a high-temperature flow for $T > \Delta/B$ and the low-temperature $T < \Delta/B$ flow. Their properties hinge on the size of the gap and *ph*-asymmetry of the TDOS. Second, they both correspond to a cascade of effective models well known from the AIM with a *ph*-symmetric band and out-of-half-filling QD. At $A = 0$ the cascade of FO-LM-SC effective models is at the center of both RG flows, while at $A \neq 0$ it takes the form of an FO-LM-FI cascade.

However, high and low $T$ cascades do not appear unimpaired. Instead, the semiconductor gap governs which RG fixed points are reached in the actual parameter setup. In detail, when the gap $\Delta$ is large enough, the $T > \Delta/B$ cascade might be interrupted even before it reaches the FO fixed point. In such a case, the $T < \Delta/B$ cascade might start in the FO regime. However, at typical values of the gap $\Delta$ the high-$T$ cascade is interrupted around the *LM* regime and the low-temperature cascade starts then consequently not in the FO regime but close to the LM regime. In any case, the RG flow is attractive for all parameter model values. Dependent on the *ph*-asymmetry, at lowest temperature scales one either reaches the SC ($A = 0$) or FI ($A \neq 0$) fixed point. Interestingly, *ph*-asymmetry introduced into the TDOS is pronounced in the high-temperature RG flow only relatively close to the threshold of $T \approx \Delta/B$.

The RG flows are thus clearly pointing toward the following effective picture. At supragap NRG temperature an ordinary Kondo-like screening happens initially, so a local moment may develop eventually. The SC (FI) regimes are typically reached only for a system with experimentally small gaps. A more realistic semiconductor gap alters the structure of the lowest many-body states. At the crossover of $T \approx \Delta/B$, a few in-gap states (presumably bound-state-like features similar to ABS states of SC-AIM) and a continuum of supragap states emerge in the flow. This newly formed effective system is then screened by the metallic lead solely at $T < \Delta/B$. Dependent on the *ph*-asymmetry of the band, we reach either a completely screened ($A = 0$) or a partially screened scenario ($A \neq 0$). The assertion regarding the formation of bound-state-like features is later confirmed by the analysis of the spectral functions.

### B. Comparison of effective behavior for gapped hosts

Since thermodynamic properties are a direct consequence of the underlying effective models, they also allow a streamlined comparison by discussing just the temperature-dependent values of thermodynamic quantities. For this we select $S_z^2$, the square of the *z*-component of impurity spin,

and $S_{\text{imp}}$, the impurity entropy. The latter is obtained as a difference of entropy between the system with and without the QD. The results are presented in Figs. 4 and 5 for $U/\Delta = 3$, $\Gamma_S/\Delta = 1$, $\Gamma_M = 0.1\Delta$, and $\Delta = 5 \times 10^{-4}B$ at varying $A$.

In Figs. 4(a) and 5(a) the thermodynamic properties of the SC-AIM+M and the AGNR-AIM+M model (10) are shown. Although the underlying physics of these models is essentially different, their effective behavior is exactly the same and follows the reentrant pattern of Sec. III A. The *ph*-asymmetry factor $\varphi$, however, governs only a quite narrow region around the gap. Thus, even at the highest induced *ph*-asymmetry ($\varphi = 0$), the ratio of the negative frequency portion of the TDOS to its positive frequency counterpart is only $\approx 1.008$ while the respective ratios for $A$ in Figs. 4(b)–4(d) or Figs. 5(b)–5(d) are $(1 + A)/(1 - A)$ and thus much larger.

Comparing first the *ph*-symmetric results of SC-AIM+M and AGNR-AIM+M to the remaining three models, we see that the Kondo temperature in Fig. 4 might be read off approximately as $T$ at which $S_{\text{imp}}$ reaches $\ln(2)/2$, which is sufficient for our purposes [60]. We notice that the Kondo temperature in Fig. 4 is roughly 10 times larger than that in Figs. 4(b)–4(d). This clearly shows the importance of states close to the gap edges for screening processes. These findings are also confirmed by analogous comparison made for $S_z^2$ from Fig. 5.

As already pointed out, the overall asymmetry of the host band in Fig. 4(a) is relatively small compared to Figs. 4(b)–4(d) and yet at $\varphi = 0$ it still increased the temperature of the transition to the strongly correlated regime by five orders of magnitude in comparison to $\varphi = \pi$. Comparable effects in the remaining three models are only possible at factors $A$ which induce very large *ph*-asymmetry into the TDOS. Although this does not impair the theoretical tools for understanding the unified nature of QPTs, the necessary large imbalance challenges possible experimental realizations, as discussed in Sec. V.

Comparison of panels (b) and (d) in Figs. 4 and 5, respectively, shows that smoothening of finite discontinuities at the gap edges has overall only a small impact on the resulting effective behavior. Nevertheless, we observe that the reentrant behavior is actually weakened at $T \approx \Delta$ (dashed-dotted line). Similar findings apply to the R-AIM+M in Figs. 4(c) and 5(c), where the effect is even stronger due to the redistributions of TDOS in more extended regions. Consequently, much larger *ph*-asymmetry in the TDOS is required to obtain comparable effects on the thermodynamic behavior. On the contrary, in AGNR-AIM+M the BCS-like singularities at the gap edges do not just modify the regions very close to the gap edges. We can thus conclude that modifications close to the gap edges play a more essential role in affecting the screening processes at $T \ll \Delta/B$ than the extended modifications present in SG-AIM and, especially, R-AIM. Moreover, we stress that decreasing $\Gamma_M \to 0$ impacts mainly the subgap temperature part of the reentrant behavior as discussed also in [52], where decreasing $\Gamma_M$ was shown to decrease the width of subgap Kondo-like features. In thermodynamic properties, this would mainly push the subgap RG fixed points and corresponding values of thermodynamic properties towards small temperatures, but the reentrancy would remain preserved.
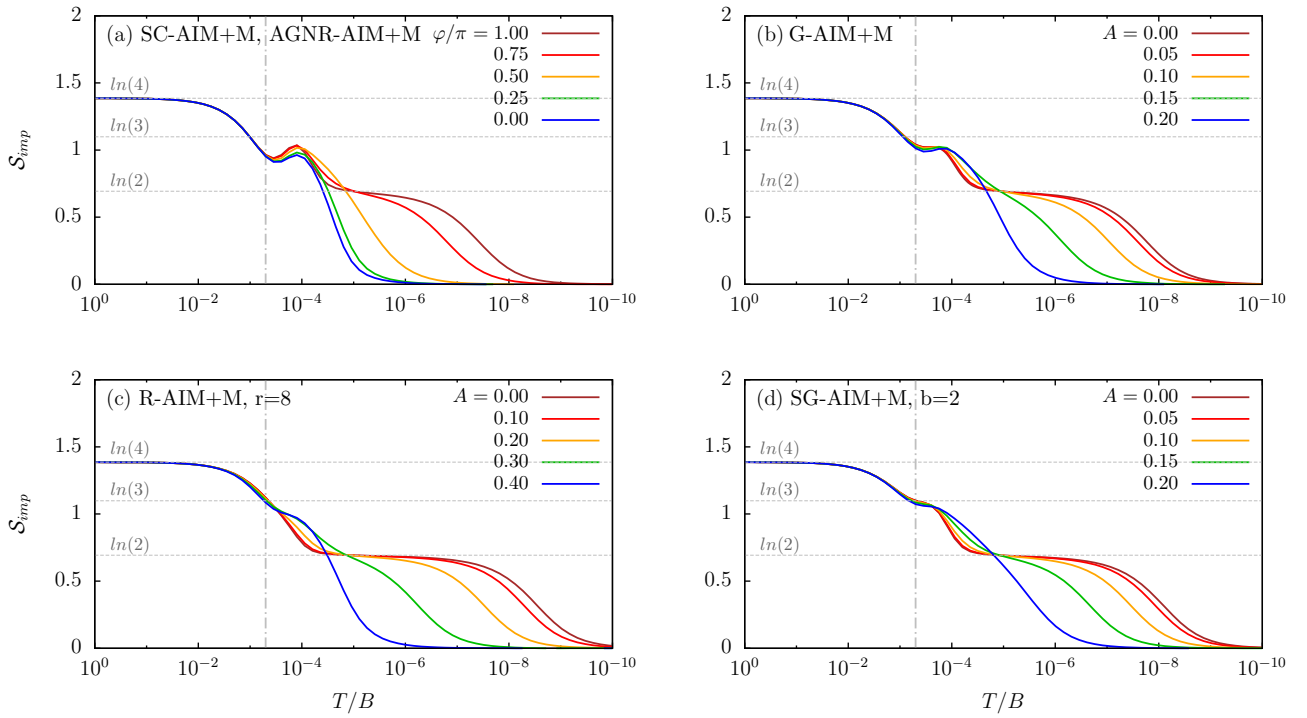
FIG. 4. (a) Impurity entropy $S_{\text{imp}}$ for SC-AIM+M and AGNR-AM+M (6) calculated at $U/\Delta = 3$, $\Gamma_S/\Delta = 1$, $\Gamma_M/\Delta = 0.1$, and $\Delta = 5 \times 10^{-4}B$ at indicated *ph*-asymmetry factors $\varphi$. Notice that $\varphi = \pi$ corresponds to the fully symmetric case while $\varphi = 0$ represents the largest possible asymmetry. (b) $S_{\text{imp}}$ for G-AIM with parameters according to (a). *ph*-asymmetry incorporated via factor $A$ with $A = 0$ being the fully symmetric case while $A = 1$ represents the largest possible asymmetry. (c) $S_{\text{imp}}$ for R-AIM with $A$ defined as in (b) and the same model parameters except of $\Gamma_S = 6.25 \times 10^{-4}$ to adjust the overall TDOS integral. Note that large asymmetry factors $A$ are required to obtain comparable shifts in thermodynamic behavior since TDOS (14) essentially depopulates large regions around the gap edges. It thus implies that an excess TDOS close to the gap edges, like in (a), is essential for modifying the behavior of the QD system at low $T$. (d) $S_{\text{imp}}$ for SG-AIM. Notice that quantitative differences to (b) are almost negligible, thus ruling out the importance of finite discontinuities for qualitative behavior.
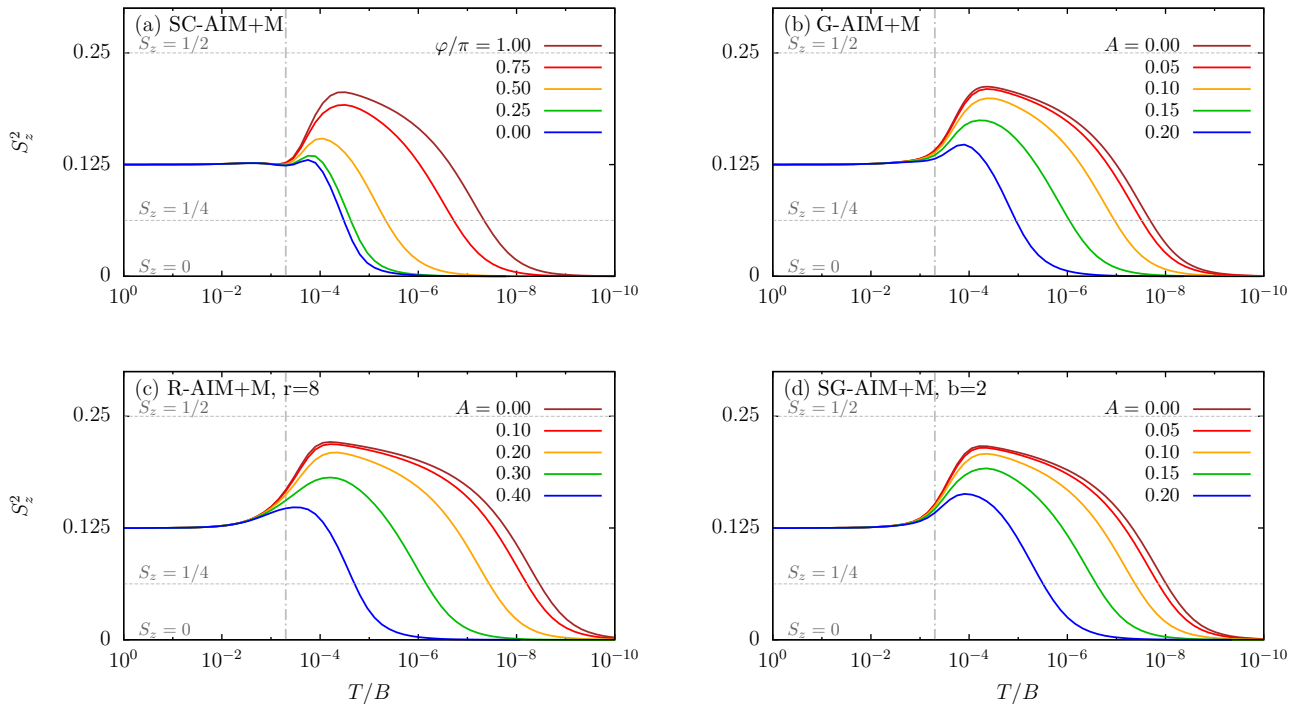


FIG. 5. Panels (a)–(d) show NRG results for $S_z^2$ at parameter values corresponding to the same panels of Fig. 4.
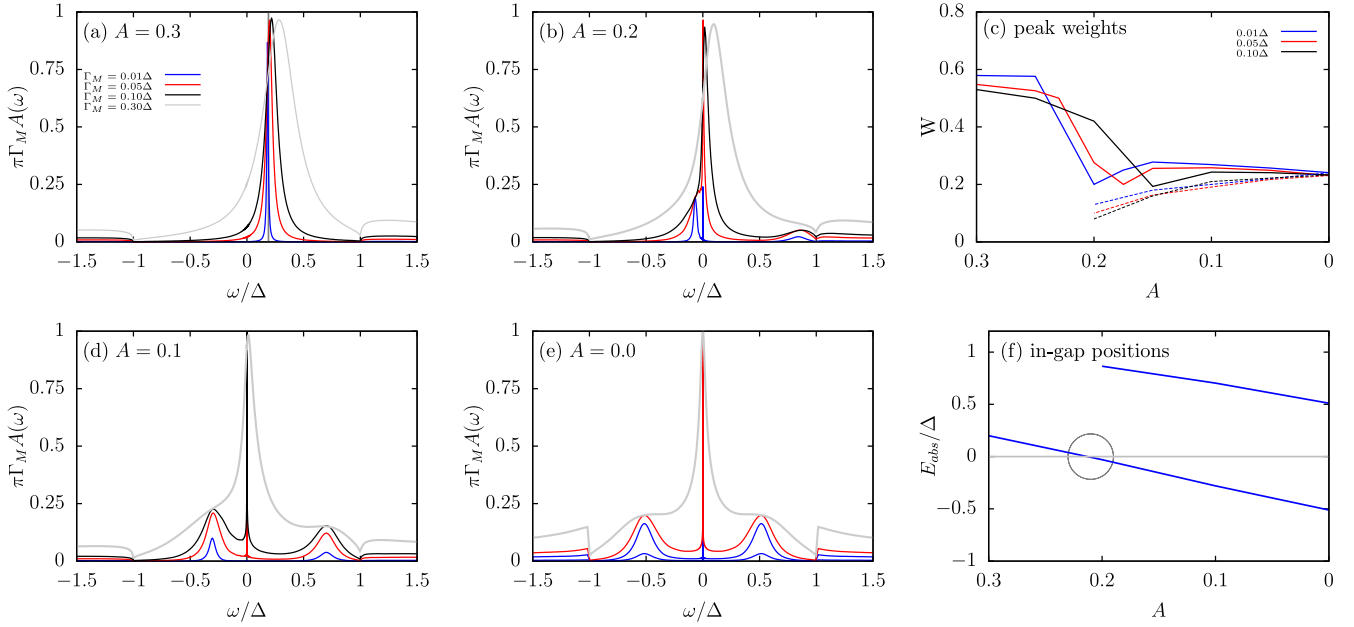
FIG. 6. (a),(b),(d),(e) The in-gap part of the spectral functions $\mathcal{A}(\omega)$ shows broadened in-gap states plotted against the Friedel sum rule for G-AIM+M at selected values of $A$ as parametric plots of $\Gamma_M$. (c) Weight $W$ of the in-gap peaks approaches a nonzero value as $\Gamma_M \to 0$. (f) $A$-dependent position of broadened in-gap states of G-AIM+M at $\Gamma_M = 0.01\Delta$. All panels have been calculated using NRG Ljubljana with $\Lambda = 2$ for $U = 3\Delta$, $\Gamma_S = \Delta$, $\Delta = 10^{-3}B$, with $2B$ being the width of the band.

At this point, we would like to stress that reentrancy, which was already reported for *ph*-symmetric AGNR-AIM in Ref. [51] and for SC-AIM in Ref. [52], is at the heart of all physical phenomena discussed here. It is deeply rooted in the presence of the gap and offers another example of behavior which seemingly contradicts the *g-theorem* [61,62]. The formation of two cascades of effective models means that successive NRG iterations lead to the supragap screening. This corresponds to the supragap Kondo-like feature discussed in [51,52], which is then, however, released to allow subgap screening processes. Such surprising behavior is, however, easily explained once we recognize that initially, the screening processes dress the original QD by inducing subgap states to the system. We explicitly confirm this in Secs. IV A and IV B. Subsequently, further screening applies to such a dressed QD with four subgap many-body states and a supragap continuum. Calculating subgap $\mathcal{S}_{\text{imp}}$ in the standard way, i.e., as the difference between the entropy of the full system and a system without the QD, leads to contributions that stem predominantly from the four lowest-lying many-body states. Initially, their screening might be insufficient, and subgap $\mathcal{S}_{\text{imp}}$ might transiently increase. Thermodynamic laws are not violated since the QD is strongly interacting and the entropy $\mathcal{S}_{\text{imp}}$ is thus not representing the entropy of a weakly perturbed system.

## IV. UNDERLYING QPTS

### A. Subgap spectroscopy of G-AIM

We have so far showed that thermodynamics properties of the gapped TDOS functions defined in Sec. II C follow the same reentrant scenario. Since the metallic electrode added to the gapped TDOS dominates the low $T$ characteristics, the ground-state properties for $\Gamma_M = 0$ can only be assessed indi-

rectly. As already discussed above, this problem is redeemed by allowing standard NRG calculations for G-AIM+M. In Figs. 6(a)–6(f), the resulting evolution of the subgap spectral functions with *ph*-asymmetry is shown for various values of $\Gamma_M$. The panels of Fig. 6 are ordered in a decreasing order in $A$ to match the corresponding $\varphi$-evolution for SC-AIM or AGNR-AIM systems. The spectral weight $W$ of the in-gap peaks slightly increases as $\Gamma_M \to 0$ and is finite even at the point of crossing the Fermi energy. The observed dip in $\mathcal{W}$ at this point seems to be a numeric artifact caused by the overlap of ABS peaks with Kondo-like features.

In detail, in the *ph*-symmetric case, i.e., $A = 0$, shown in Fig. 6(e), a symmetric subgap spectral function $\mathcal{A}(\omega)$ is observed. The Kondo anomaly at $\omega = 0$ is accompanied by two subgap peaks at $\omega/\Delta \approx \pm 0.5$ when $\Gamma_M \lesssim 0.1\Delta$. These cannot be understood as Hubbard peaks due to the mismatch in the position and traces of Hubbard-like satellites in the supragap region [63]. Increasing *ph*-asymmetry forces an excess TDOS in its negative (particle) domain, which deforms the spectral function. For $A \lesssim 0.2$ the position of the Kondo peak stays at $\omega \approx 0$, while subgap peaks shift towards positive frequencies. At critical *ph*-asymmetry, i.e., $A_c \approx 0.2$, the electronlike side peak is pushed against the gap edge at $\omega = \Delta$ and its holelike counterpart crosses the Fermi energy; see Fig. 6(c). At this point, the central Kondo peak disappears due to the increased charge fluctuations. In terms of fixed points and effective models, this scenario is linked to reaching the effective FI regime by skipping VF and LM regimes. Increasing $A$ beyond $A_c$ results in a further shift of the in-gap peak toward the $\omega = \Delta$ position without any Kondo-like maxima being present. The second in-gap peak vanishes soon, and it is impossible to distinguish whether it traverses into the continuous part or merges with the gap edge at $\omega = \Delta$ as determination of the spectral weight becomes extremely

biased. The regime observed at $A < A_c$ is thus in full analogy to the $\pi$-like regime of AGNR-AIM+M, while for $A > A_c$ characteristic signs of the 0-like regime are evident [50].

Overall, we obtain subgap spectral behavior that is in complete analogy to the AGNR-AIM+M of Fig. 2, where the properties of the ground state at $\Gamma_M = 0$ may be inferred from the SC-AIM solution. Consequently, at $A = 0$ we can infer for G-AIM a doublet ground state which is in accordance with results of various perturbative and nonperturbative results [44,45,47–49]. The crossing of the broadened in-gap peak with Fermi energy at $A_c = 0.2$ indicates an underlying QPT for $\Gamma_M = 0$. Again, the nature of the ground state cannot be read off directly, but comparison of Fig. 6 with Fig. 2 clearly points to a doublet-singlet ground-state transition at $A_c$.

Note that the number of subgap peaks and their asymmetric position with respect to Fermi level, as shown in Fig. 6(f), contrasts the SC-AIM case. However, the reason for the presence of symmetric pairs of ABS states in SC-AIM is the underlying formation of Cooper pairs ensuring that the energy eigenstates have half-to-half particle and hole character. Consequently, pairs of ABS states in spectral functions represent one-particle excitations of the ground state—and this is reflected in the characteristic picture showing pairs of ABSs in the normal spectral function. Apart from this symmetry, which is directly linked to the superconducting nature of the host band, the QPT of G-AIM obtained by varying $A$ is the same as that of AGNR-AIM or SC-AIM with QD at half-filling.

Let us conclude this section by noting that the above discussed critical $A$ is $U$-dependent. The relevant SC-AIM as well as SC-AIM+M studies [50,52] imply that there is actually a threshold $U$ above which the 0-like phase is not realized at all. The whole phase space is then dominated by the $\pi$-like regime, and at $\Gamma_M = 0$ a distinct $\pi$ phase is observed. Similarly, while qualitatively all systems behave essentially the same, variations of the TDOS functions can significantly influence particular details, e.g., the evolution of the subgap states. We briefly discuss this in the following section.

### B. Subgap spectroscopy for gapped host bands

While not explicitly presented here, the TDOS functions (14) and (13) show a similar parametric dependence of spectral functions to that for G-AIM discussed above. Thus, only two distinct phases at $\Gamma_M = 0$, namely the 0 and the $\pi$, are present. When a metallic electrode is added, the distinct properties of the two phases are blurred out and instead two regimes, termed 0-like and $\pi$-like regimes, appear [50]. In detail, the $\pi$-like regime is for finite but small $\Gamma_M$ signaled by the appearance of a central Kondo-like peak and two in-gap peaks. These are asymmetrically placed within the gap for any $A \neq 0$, i.e., they do not form a symmetrized pairs known from the SC-AIM due to the reasons discussed above. When a critical value of $ph$-asymmetry is reached, the charge-fluctuations take over and suppress the central peak. For models with a weakly hybridized metallic electrode, one reaches the 0-like regime, which is marked by one in-gap peak being present in the positive frequency region of the gap while none is present in the negative frequency gap region. A second peak is pushed toward the gap edge at $\omega = \Delta$, and although it

does not completely vanish for $\Gamma_M \neq 0$, it is highly suppressed and practically invisible in the background features. We also stress that for $0 > A > -1$ we would observe the same motion of subgap peaks in a reversed direction toward negative frequencies.

Instead of showing the whole spectral functions, we extract the subgap peak positions and plot these in Fig. 7. In all cases, the same qualitative dependence with $ph$-asymmetry, including the crossings of in-gap states with Fermi energy, is observed. Arguably, the crossing accompanied by the corresponding QPT might not happen always at experimentally meaningful values of $\varphi$ for AGNR-AIM and of $A$ for G-AIM, R-AIM, and SG-AIM. Nevertheless, they still point toward the same singlet-doublet properties of the studied TDOS systems. In Sec. V, we also discuss other experimentally and physically more straightforward ways to induce QPTs.

In this respect, we note that from all TDOS cases studied here, the R-AIM case requires the highest amount of $ph$-asymmetry to drive the system into the 0-like regime, as Fig. 7 clearly demonstrates. Above a certain threshold value of $U$ there is not enough $ph$-asymmetry to induce a QPT as $|A|$ is strictly smaller than 1. We note that a similar situation is also observed without metallic leads for SC-AIM, where the $\varphi$-dependent $ph$-asymmetry of quasiparticles $w$ is bound by $\varphi = 0$. For $U$ above a certain threshold, SC-AIM remains always in the $\pi$ phase. Nevertheless, we would like to stress that such scenarios are not generic and depend clearly in a multiparametric way on the exact realization. This applies to both superconducting and semiconducting host bands.

Let us now inspect the possibility of naive interpretation of the observed broadened in-gap peaks as Hubbard satellites. For $U/2 > \Delta$ this can be ruled out by observing traces of Hubbard peaks at $\pm U/2$ of the supragap spectral functions and their $A$-dependent positions. Additionally, also the RG flow and the resulting thermodynamic effective behavior established that in all four general cases, reentrant behavior appears. The low-$T$ behavior leads then to the formation of broadened in-gap peaks that can be formally understood as effective Hubbard peaks, but as shown in Ref. [52] they do not follow from the bare values of $\Gamma_M$ and $U$, and they are heavily influenced by supragap properties that govern their position.

However, for $U/2 < \Delta$ our current approach is insufficient and a dedicated NRG solution for $\Gamma_M = 0$ is required. The reason lies in the fact that Hubbard peaks present in the supragap portion of the spectral function weaken the reentrant character of the flow, and charge oscillations influence directly the subgap spectral function with in-gap peaks becoming indistinguishable from $ph$-asymmetry-dependent Hubbard peaks. They might therefore be just an artifact of augmenting the gapped TDOS functions by metallic leads, and true in-gap peaks might remain hidden behind the strong Kondo-like signal as they are expected to lie close to the Fermi energy.

Related restrictions are also observed for R-AIM and SG-AIM in certain parameter regimes as discussed thoroughly in Appendix A 5. Here, Fig. 12 clearly shows that by decreasing $r$ of R-AIM or increasing $b$ of SQ-AIM, we may effectively push some of the in-gap peaks outside of the gap region. While in R-AIM they seem to simply merge with the continuous part, in SG-AIM they remain noticeable, albeit determining their
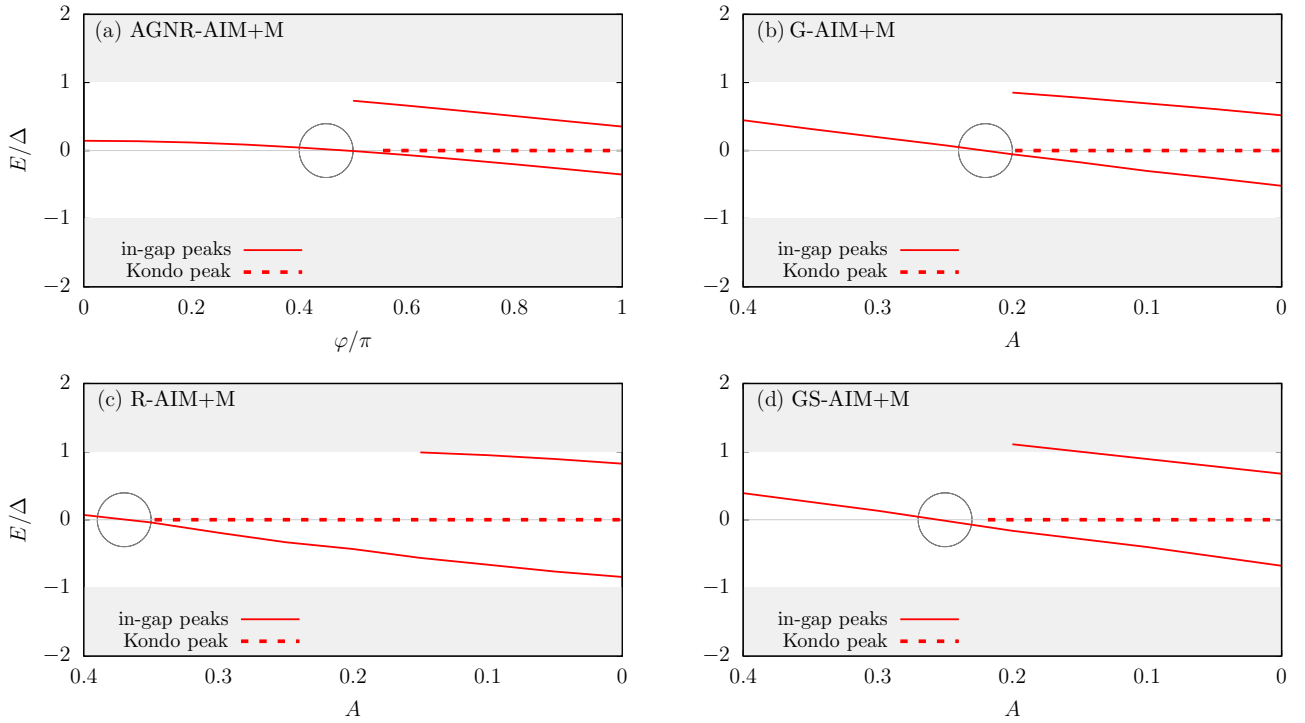
FIG. 7. $\varphi$-dependent subgap spectroscopy for AGNR-AIM+M (a) and $A$-dependent subgap spectroscopy for G-AIM+M in (b), R-AIM+M in (c), and GS-AIM+M in (d). All models calculated at $U/\Delta = 3$, $\Gamma_S/\Delta = 1$, $\Delta = 5 \times 10^{-4}B$, and $\Gamma_M = 0.1\Delta$. Except for R-AIM+M, $\Gamma_S/\Delta = 6.25 \times 10^{-4}$ to adjust for the overall TDOS integral. For AGNR-AIM+M, $\varphi = \pi$ represents the fully symmetric case while $\varphi = 0$ is the most $ph$-asymmetric scenario. For G-AIM+M, R-AIM+M, and GS-AIM+M, $A = 0$ represents the fully symmetric case while $A = 1$ induces the largest possible asymmetry.

weights is difficult because of the continuous background (the corresponding spectral weights are thus not shown). Such an escape is then bound from above by $U/2$ corresponding to the position of Hubbard satellites. In such regimes, it is not only difficult to reliably extrapolate for possible QPTs, but even the nature of the in-gap peaks is hard to stipulate about. Taken together, the subgap spectroscopy of R-AIM and SG-AIM may point toward breaking of the equivalence to SC-AIM in certain parameter regimes.

## V. POSSIBLE EXPERIMENTAL REALIZATION OF THE SINGLET-DOUBLET TRANSITION IN SEMICONDUCTING HOST BANDS

In this paper, we have postulated several shapes of TDOS functions and verified that all can support the singlet-doublet QPTs. The existence of QPTs thus hinges more on the presence of the spectral gap than on the exact details of the TDOS. Consequently, we expect that quite a large class of setups (some already under investigation) might be promising candidates for experimental scrutiny of the results presented herein.

In this respect, nanostructure, e.g., a single molecule or a carbon nanotube, absorbed on (or connected to) a semiconducting surface represents a generic layout [64]. In principle, the subgap states should be directly detectable by high-resolution energy spectroscopy using tunneling probes. These techniques, in addition to their high precision, allow for some control of the heterostructure parameters, such as the hy-

bridization or level energy [5,65,66]. In practice, intra-atomic interactions between the nanosystem and the substrate(s) might interfere with the simple single spin-orbital picture used in the present paper. As an example, one can mention the experiment in Ref. [64] where a layer of semiconducting graphene on a metallic substrate was studied. This seems to be an ideal realization of the systems presented herein. However, the electronic transparency of graphene caused the nanosystem to develop strong spin interactions with the metallic substrate. Consequently, it did not inherit many of the semiconducting properties of graphene, and any traces of possible in-gap features as discussed in the present paper have been lost. Nevertheless, such effects are not fundamentally hindering electron spectroscopy in semiconductor devices. As already proven for the ABS states in various types of Josephson junctions, high-resolution scanning tunneling images can be acquired [7–9,11].

Let us therefore focus on the fundamental constraint given by the ratio of $U/\Delta$. As discussed above, a moderate value is required. In the case of strong interaction, $U \gg \Delta$, the subgap states are pushed to the gap edge where they become indistinguishable from the continuum. In the other limit, $U \rightarrow 0$, they move to the close vicinity of the Fermi level, where they overlap and might even be mistaken for, or can merge with, other types of resonances, e.g., the Kondo anomaly (or Majorana states). This would again complicate the observation of the Fermi-level crossing.

However, semiconductors typically have larger values of the gap parameter. Thus, larger absolute values of $U$ are

needed. In the case of superconducting quantum dot realizations, for which singlet-doublet QPTs have already been studied experimentally, the typical charging energy, made, for example, from the carbon nanotube, is on the order of meV, and the gap is on the order of hundreds of $\mu$eV (e.g., 0.17 meV for aluminum leads) [10,11,67].

Nevertheless, in principle even semiconductors with very narrow gaps can be synthesized. For example, mercury-cadmium telluride, used in infrared detectors, allows us to tune the band gap from zero up to a few electronvolts [68]. Heterostructures consisting of organic molecules absorbed on the semiconducting surface might also represent good alternatives. For example, the recent realization of porphyrin-based magnetic molecule TBrPP-Co on AGNR substrate [64] has $U$ on the order of a few eV, while the AGNR band gap was 1–2 eV in size depending on the width of the absorbed molecule.

To our knowledge, no fundamental obstacles are present for detecting subgap states on top of semiconductor surfaces. However, unlike in superconductors where the phase bias controls the underlying *ph*-asymmetry of the $w$ Bogoliubons, one cannot exert such tuning in semiconductors. Some materials, like AGNR, allow us to adjust the gap by external electric fields but not the *ph*-asymmetry of the band. We therefore stress that the parameter $A$ was used in the present paper solely to model theoretically the singlet-doublet QPTs in close analogy with superconducting realizations. Experimentally, for semiconducting substrates, the more viable concept is that of gate voltage on the QD. Driving it out of half-filling is an analogous process to the inclusion of *ph*-asymmetry into the TDOS. Other alternatives include changing the size of the gap by tuning the substrate or varying hybridization by lifting the molecule via the STM tip. Experiments with carbon nanotubes seem to offer another pathway for detection of singlet-doublet QPTs in semiconductor host bands. To this end, one may electrostatically control the coupling of the carbon nanotube to the leads. Increasing the hybridization of the nanotube to the semiconductor would bring the system out of the doublet into the singlet ground state as already performed in superconductor QD devices [69].

## VI. CONCLUSIONS

In this paper, we have analyzed half-filled QDs coupled to four general classes of semiconductor TDOS functions (see Fig. 1) in regard to the existence of eventual singlet-doublet QPTs. To allow for an unbiased and standard NRG approach without temperature truncations, as employed in Refs. [47,48], we have augmented the gapped host bands by a weakly hybridized metallic electrode. The thermodynamic behavior conformed to the underlying cascade of reentrant effective models that develop in two sequences. One is present at high and the other at low temperatures. Each sequence of effective models was established to follow those of AIM with out-of-half-filling QD, albeit we explicitly demanded half-filled QDs.

Since metallic electrons enforce a singlet ground state into the system, we have observed only broadened in-gap features at $\Gamma_M \neq 0$, and the nature of QPTs could only be deduced indirectly. However, we stress that all of these limitations have
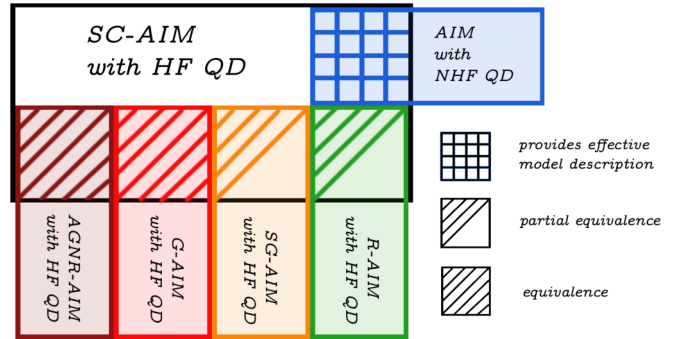


FIG. 8. The main conclusion regarding the presence of singlet-doublet QPT in QDs coupled to gapped host bands of various properties is summarized as overlaps between the colored boxes representing a given model, i.e., AGNR-AIM with half-filled (HF) QD (brown), G-AIM with HF QD (red), SG-AIM with HF QD (orange), and R-AIM with HF QD (green), and the large box representing SC-AIM (black). AIM with out-of-half-filling (NHF) QD (blue box) provides an effective description. For R-AIM and SG-AIM we have shown in Appendix A 5 that our present approach with augmenting the host band with a metallic electrode to perform standard NRG cannot lead to a reliable conclusion in some parameter regimes.

been compensated by obtaining unbiased and numerically exact quantities.

In general, all four investigated classes may support the singlet-doublet QPTs. Their physical origin lies in the presence of a gap and the *ph*-asymmetry in the TDOS. Our main conclusion can thus be summarized by Fig. 8 in the following way. A prototypical SC-AIM case and all four general classes of semiconductor support the presence of singlet-doublet behavior. The spectral equivalence is strong for the G-AIM and AGNR-AIM systems since these possess discontinuities at the gap edges. However, once the discontinuities are smoothed out, as in the R-AIM or SG-AIM cases, the equivalence becomes weaker. In-gap peaks known from SC-AIM may escape into the continuum as shown in Appendix A 5, and their properties become increasingly similar to the ordinary Hubbard peaks. In such cases, we cannot confirm or exclude the presence of QPTs as the nature of the ground states cannot be reliably extrapolated from models augmented by metallic electrodes. Further investigation, therefore, requires a genuine RG approach to gapped host bands, which is currently being developed. In Fig. 8 we indicate this by stating only a partial equivalence.

Crucially, the presence of in-gap states in any of the gapped systems in their realization with weakly hybridized leads is always signaled by reentrant effective-temperature behavior. This is governed by AIM with a flat density of states but an out-of-half-filling QD. As explained in Sec. III A, this is expected in the high-temperature part of the reentrant behavior, which is indeed marked by the presence of *ph*-asymmetry in the supragap part of the TDOS. In the low-temperature part, a sequential nature of the flow can be interpreted as adding a flat metallic TDOS to the effective model of AIM with QD out-of-half-filling. Reentrant effective behavior follows, therefore, a cascade of effective models known from AIM with QD out-of-half-filling. This is a precursor for the recently

introduced concept of reentrant Kondo behavior [50–52] but also for the appearance of singlet-doublet QPTs.

We stress that in the present paper, *ph*-asymmetry was introduced to serve a theoretical purpose of showing that doublet-singlet QPTs exist in general classes of gapped host bands and are analogous to the well understood effects in superconducting realizations. The *ph*-asymmetry was thus introduced into the TDOS to match its generation in the SC-AIM case via tuning of the phase drop between two superconducting leads, which, as shown in Ref. [50], controls the *ph*-asymmetry of the underlying Bogoliubons $w$. In semiconducting bands, an analogous method requires that we tune *ph*-asymmetry in host bands, which is hard to achieve in practice. Furthermore, the *ph*-asymmetry required to force the resulting system out of the doublet ground state might be too large for experimental realizations. Instead, as proposed in Sec. V, an experimental observation should rely on taking the QDs out of their half-filled point, which can be done by using appropriate gating, which is a scenario with a much larger phase space that shall be analyzed separately. In addition, the obtained data are of importance for benchmarking the NRG algorithm for gapped host bands, which we are currently being developed.

## APPENDIX

### 1. NRG

All models considered in the main text are tractable within the standard one-channel NRG with host band interactions expressed via the corresponding TDOS, which at $\Gamma_M \neq 0$ provide all necessary coefficients to construct the Wilson chains of the corresponding NRG calculations [37,70]. For SC-AIM ($\Gamma_M = 0$), conventional NRG solutions are available for subgap properties [12,54], however even here artificial truncations are required to reconstruct the supragap spectral functions [41]. For the $\Gamma_M \neq 0$ cases, the NRG Ljubljana code [71] with the intertwined *z*-discretization according to the scheme introduced by Žitko and Pruschke [72] was thus employed with the discretization parameter $\Lambda = 2$ and $z = n/10$ with $n \in \{1, \ldots, 10\}$ with subsequent application of the so-called self-energy trick to the spectral functions [73].

While dynamic properties, like spectral functions, might nowadays be obtained with great accuracy [37], the original NRG idea of obtaining a temperature-dependent effective description from the underlying microscopic model, as presented in the seminal papers of Refs. [35,36], is to a great extent marginalized. Yet, all thermodynamic and spectral properties are relatively straightforward consequences of specific subspaces of the QD being effectively projected out in the given fixed points of NRG transformations. These can be directly read off from the corresponding flow diagrams. Because the effective behavior constitutes a major unifying feature for the gapped TDOS functions studied here, we briefly review this topic. Further details, including the definitions of the effective Hamiltonians and calculation of linear corrections to these, can be found in Refs. [35,36].

### 2. The effective behavior of AIM

While half-filling of the QD was kept during all presented calculations and only the *ph*-asymmetry of the host bands was varied, the presence of the gap in the host bands actually forces a previously not understood effective behavior which relates to the out-of-half-filling AIM with a flat TDOS—a case already treated by Wilson *et al.* [36]. We thus briefly review the standard NRG results obtained in the seminal papers of Refs. [35,36]

In accordance with Ref. [36], the RG flow of the energy eigenstates $E_n$ for even NRG iterations is inspected. The corresponding RG flow in Fig. 9(a) shows the system approaching four fixed points. For $T/B \approx 1$, the free-orbital (FO) fixed point appears first. Lowering $T/B$, a sequence of valence-fluctuation (VF), local-moment (LM), and finally the frozen-impurity (FI) fixed point (out of half-filling) emerges. At half-filling, the strong-coupling (SC) fixed point appears instead of FI. They all can be read off from the flow via characteristic values of quantum numbers and $E_n$ of the low-lying levels [74].

The numerical positions of $E_n$ in the FO, VF, LM, and SC regimes depend only on $\Lambda$ and are thus independent of the model parameters [35,36]. The FI fixed point is the only regime in which model parameters play a role. Nevertheless, for $\delta \approx 0$ it is marked by splitting of rescaled $E_n$ around their SC positions as shown in Fig. 9. Taking $\delta \to \infty$, the splitting becomes extremely strong. The lowest doublet state approaches the singlet ground state. Note that the VF and LM fixed points can be skipped at certain values of $\varepsilon_{\text{dot}}$, but the FI or SC fixed points are always present for $\delta > 0$ and $\delta = 0$, respectively. It is important to stress that systems close to RG fixed points show universalities, as shown in Refs. [35,36], which thus offers a simple yet precise characterization.

Let us now briefly review the effective behavior in the FO, VF, LM, FI, and SC regimes. The FO fixed point belongs to the most trivial ones because the system behaves as a free Anderson impurity that is disconnected from the host band. It can be obtained by setting $\Gamma = U = \varepsilon_{\text{dot}} = 0$. The VF fixed point that might follow after the FO fixed point appears only at certain values of $\varepsilon_{\text{dot}}$ and corresponds to the situation where doubly occupied states on the QD are effectively projected out, and as such it corresponds to $\Gamma = \varepsilon_{\text{dot}} = 0$ and $U \to \infty$. The LM fixed point connects AIM to the Kondo model where the doubly and zero occupied states of the QD are projected out. The antiferromagnetic coupling $J$ of the effective Kondo model can be read out from the corresponding NRG calculations. In the final stages of NRG flow of the half-filled case, we always observe the SC fixed point while out-of-half-filling the FI emerges. In FI, all states except of the unoccupied QD are projected out when $\delta > 0$ [75]. In the SC fixed point,
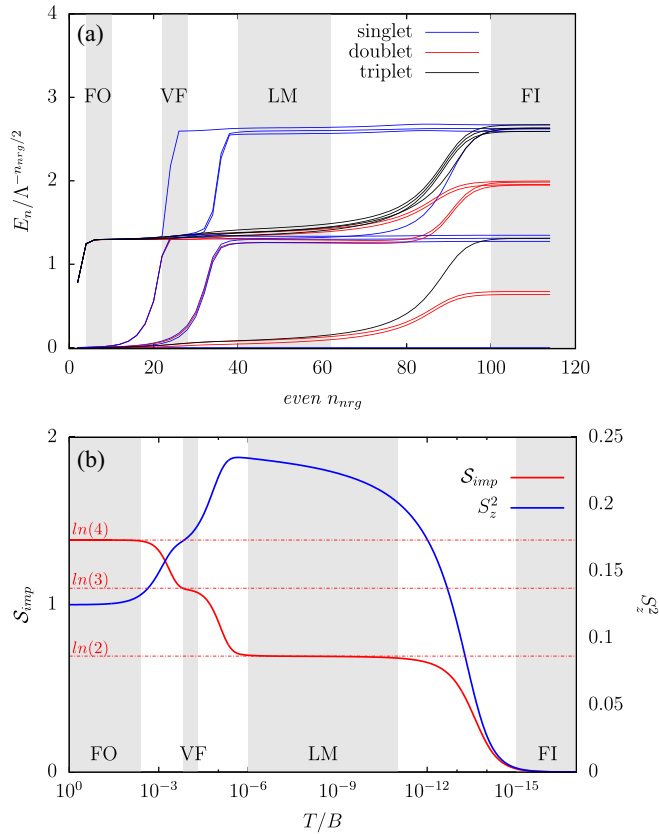
FIG. 9. (a) Flow of rescaled eigenenergies $E_n$ during the even NRG iterations $n_{\text{even}}$ of the asymmetric AIM with $U/B = 10^{-3}$, $\Gamma_M/B = \pi/2 \times 10^{-6}$, $\varepsilon_{\text{dot}}/B = -2 \times 10^{-4}$, and $\Lambda = 2$. Free orbital (FO) fixed point for $n_{\text{NRG}} < 10$, valence-fluctuation (VF) fixed point for $20 < n_{\text{NRG}} < 26$, local-moment (LM) fixed point for $40 < n_{\text{NRG}} < 64$, and frozen-impurity (FI) fixed point for $n_{\text{NRG}} > 100$. (b) Temperature dependence of the impurity entropy $\mathcal{S}_{\text{imp}}$ (red line) and $S_z^2$ expectation value (blue line). In the FO regime, the impurity behaves as four fluctuating levels, i.e., $\mathcal{S}_{\text{imp}} = \ln(4)$, while in the VF regime the doubly occupied state is effectively projected out and the impurity behaves as a three-level system with $\mathcal{S}_{\text{imp}} = \ln(3)$. Proceeding further in the flow, zero occupied states are effectively projected out leaving only two levels left, i.e., $\mathcal{S}_{\text{imp}} = \ln(2)$. Finally, at very low $T$, FI fixed point means that the impurity is effectively frozen, thus leaving $\mathcal{S}_{\text{imp}} = 0$.

the QD freezes down to a single state, and this state is a specific linear combination of singly occupied QD states. The resulting effective model resembles then the free-electron Hamiltonian. The impurity in the different regimes behaves thus effectively as an ensemble of four (FO), three (VF), two (LM), and one (FI,SC) fluctuating state with the resulting entropy values $\ln(4)$, $\ln(3)$, $\ln(2)$, and 0, respectively. In between the various regimes, smooth crossovers are observed as shown in Fig. 9(b) (red line). Fluctuations of the $S_z$ projection of spin onto the $z$ axis follow correspondingly as shown in Fig. 9(b) (blue line).

### 3. RG flow of *ph*-symmetric G-AIM

In Fig. 10 we present the RG flow of rescaled $E_n$ for G-AIM with $A = 0$ (*ph*-symmetric TDOS) at three selected

values of $\Delta$. In all cases, the flow consists of two sectors that connect approximately at $n_\Delta = -2\ln\Delta/\ln\Lambda$, where the energy resolution of NRG iterations reaches approximately $\Delta/B$. In Fig. 10, this is marked by vertical dash-dotted lines. For NRG iterations $n_{\text{NRG}} < n_\Delta$ we observe the high-$T$ portion of the flow that abruptly changes the character at $n_{\text{NRG}} = n_\Delta$ where it transits into the low-temperature behavior observed for $n_{\text{NRG}} > n_\Delta$.

The $T > \Delta/B$ portion of the RG flow is in one-to-one correspondence with that of the ordinary AIM with flat TDOS and QD at half-filling. Let us note that here, only the FO effective regime is clearly present (marked as FO1 in Fig. 10) for all selected values of $\Delta$, while only at $\Delta = 5 \times 10^{-6}B$ do the first traces of the high-temperature strongly coupled regime (SC1) show up [see, for example, the local minimum at $T/B \approx 10^{-5}$ in Fig. 10(f)]. Due to the selected values of $U/\Delta = 3$ and $\Gamma_S/\Delta = 1$, the LM fixed points are completely skipped. The numerical calculations for even smaller $\Delta$ as presented here are challenging. Nevertheless, from the evolution of $E_n$ flow with decreasing $\Delta$ one can extrapolate that at very small values of $\Delta$ the system can reach the high-$T$ strongly coupled regime SC1. This is in compliance with predictions based on the results presented in Ref. [51] for the AGNR-AIM+M case and in Ref. [52] for the SC-AIM+M case.

However, regardless of the existence of the high-temperature SC regime, we observe at $n_{\text{NRG}} \approx n_\Delta$ an abrupt change into a different effective mode that is caused by the reentrancy in analogy to the AGNR-AIM+M [51] and SC-AIM+M [52]. At very small $\Delta$ values the low-temperature portion of RG flow initially develops traces of the free orbital regime (FO2). At values $\Delta \approx 10^{-7}B$ the complete chain of effective behavior is expected. In detail, at high $T$ the initial FO1 regime goes over into the SC1 regime, which is then abruptly turned back into a low-temperature FO2 regime. Consequently, a cascade of the low-temperature local moment (LM2) regime followed by the final low-temperature strongly coupled (SC2) behavior can be observed. This can be attributed to a fully developed reentrant Kondo behavior, and it indicates a possible appearance of two Kondo effects at two temperature regimes [51,52] $T_1 > \Delta/B$ (high temperature) and $T_2 < \Delta/B$ (low temperature). However, the experimental observation for the semiconducting TDOS function is challenged by stringent conditions similar to the ones discussed in Ref. [52] for SC-AIM as shown in Sec. III B.

Let us now demonstrate the temperature-dependent effective behavior using the thermodynamic properties shown in Figs. 10(b), 10(d) and 10(f). As explained in Appendix A 1, particular degrees of freedom of the QD are effectively projected out close to the RG fixed points. For example, by comparing the FO1 regime of Figs. 10(e) and 10(f) with the onset of the FO2 regime at $T/B \lesssim \Delta$ we see that $\mathcal{S}_{\text{imp}}$ reaches the value of $\ln(4)$ at two very distinct temperatures. The QD can then be understood as an effective system of four states. Similarly, in LM2 the QD behaves effectively as a two-state system with single electronic occupation. In the end, QD may be effectively quenched to a single level at $T/B \gtrsim \Delta$ and then once again at $T/B \ll \Delta$ when sufficiently low $\Delta$ values are set as indicated in Fig. 10(f). This is in line with the effective behavior deduced from the flow of the rescaled $E_n$. Spin fluctuations $S_z^2$, presented in
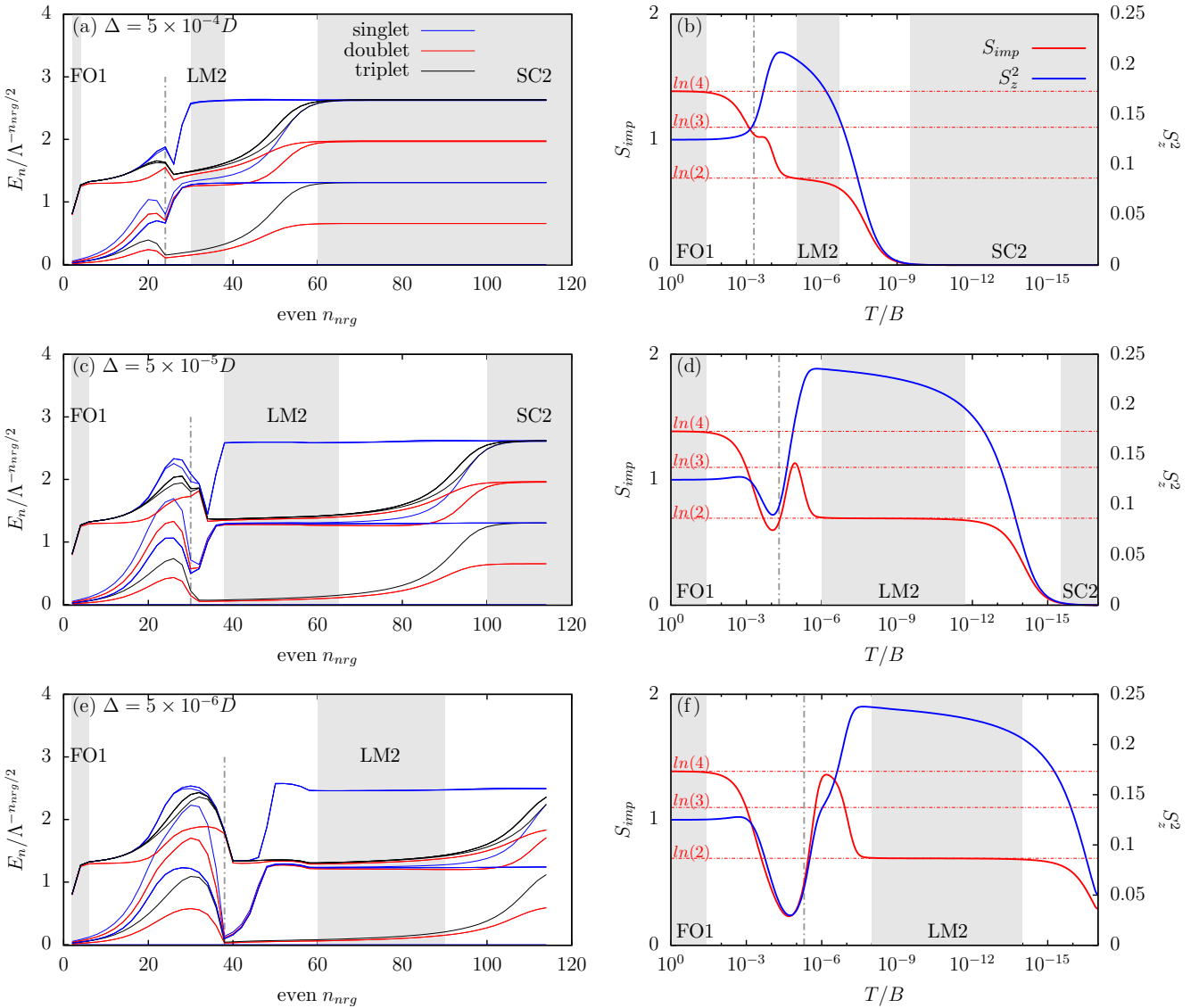
FIG. 10. (a) Flow of rescaled $E_n$ during the iterative NRG calculation of G-AIM+M with $U/\Delta = 3$, $\Gamma_S/\Delta = 1$, $\Gamma_M\Delta = 0.1$, $\Delta = 5 \times 10^{-4}B$, and $A = 0$ and $\Lambda = 2$. (b) Temperature dependence of the impurity entropy $S_{\text{imp}}$ and $S_z^2$ for the same parameters as in panel (a). (c) Flow of rescaled eigenenergies $E_n$ during the iterative NRG calculation of model (12) with parameters as in panel (a), only $\Delta = 5 \times 10^{-5}B$. (d) Temperature dependence of the impurity entropy $S_{\text{imp}}$ and $S_z^2$ for the same parameters as in panel (c). (e) Flow of rescaled eigenenergies $E_n$ during the iterative NRG calculation of model (12) with parameters as in panel (a), only $\Delta = 5 \times 10^{-6}B$. (f) Temperature dependence of the impurity entropy $S_{\text{imp}}$ and $S_z^2$ for the same parameters as in panel (e). The reentrant nature of the flow is apparently visible, the flow of $E_n$ at high $T$ is initially in the free orbital regime (FO1), and only in panel (e) are traces of the strongly coupled high-$T$ regime (SC1) visible. The dash-dotted line separates the beginning of the low-$T$ flow, which might experience the low-$T$ free orbital (FO2) regime as in panel (e) that continues into the local-moment (LM2) regime and finally flows into the strongly coupled regime (SC2) for all $\Delta$ values. The thermodynamic properties have the corresponding behavior of the fixed-point regimes.

Figs. 10(b), 10(d) and 10(f) by a blue line, support the same conclusions.

## 4. RG flow of *ph*-asymmetric G-AIM

Above, we have established an equivalence of G-AIM at $A = 0$ to the half-filled AIM with a flat TDOS in terms of RG flow. Here, we investigate the case with finite *ph*-asymmetry by selecting $A = 0.1$. The resulting RG flow of rescaled eigenenergies $E_n$ is shown in Fig. 11. Once again, at $n_\Delta \approx -2 \ln \Delta / \ln \Lambda$ the flow separates into high- and low-

temperature portions, which, however, differ qualitatively from the $A = 0$ case due to the presence of *ph*-asymmetry in the TDOS. Most importantly, valence-fluctuation and frozen impurity regimes of AIM with out-of-half-filling QD appear that are accompanied by the corresponding values of $S_{\text{imp}}$ and $S_z^2$.

The resulting reentrant temperature behavior is thus marked by a cascade of effective models known from the AIM with out-of-half-filling QD. In the high-temperature part, the free orbital regime FO1 emerges but the valence-fluctuation regime is skipped as before (due to the choice of $U$), and
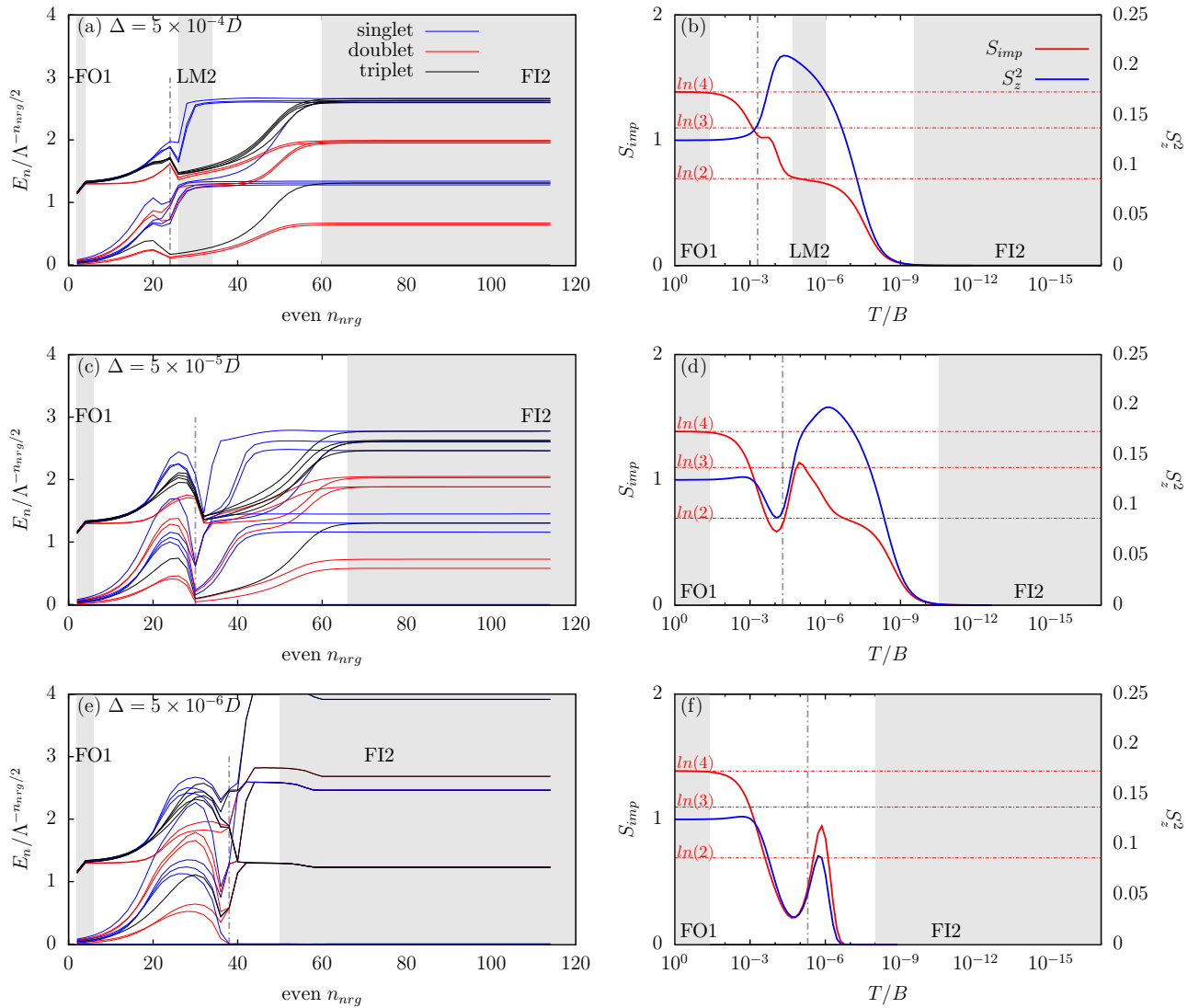
FIG. 11. Panels (a)–(f) correspond to their counterparts in Fig. 10 with only the *ph*-asymmetry factor set to $A = 0.1$. Reentrant nature of the flow is preserved also for G-AIM with *ph*-asymmetry, but the resulting effective regimes correspond to AIM with flat TDOS and QD out-of-half-filling. Thus, the flow of rescaled $E_n$ at high $T$ is initially in the free orbital regime (FO1); only in panel (e) are traces of the frozen-impurity high $T$ regime (FI1) visible. The dash-dotted line separates the beginning of the low-$T$ flow, which might experience the local-moment (LM2) regime and finally flows into the frozen-impurity regime (FI2) for all $\Delta$ values. The thermodynamic properties correspond to their effective models as discussed in Fig. 9.

only at very small $\Delta$ values [see Fig. 11(e)] are traces of the frozen impurity regime FI1 visible. The effective projection of several levels of the QD is then abruptly lifted at $T \approx \Delta/B$, where the system can go either directly to the low-temperature local-moment regime LM2 for large $\Delta$ as observed in Fig. 11(a) or at moderate $\Delta$ values to the low-temperature free orbital regime FO2. However, at sufficiently small $\Delta$ values, the low-temperature frozen impurity regime FI2 is reached immediately; see Fig. 11(e). The corresponding thermodynamic properties [Figs. 11(b), 11(d) and 11(f)] are then in accord with the temperature-dependent effective behavior that follows from the $E_n$ flow analysis.

The deviation from the $A = 0$ scenario is clearly dependent on the size of $\Delta$. In Figs. 11(a) and 11(b), at $\Delta = 5 \times 10^{-4}B$, we see negligible differences compared to the results in Figs. 10(a) and 11(b). Nevertheless, the flow of rescaled

$E_n$ clearly shows energy splittings around the corresponding *ph*-symmetric values—a behavior that persists even to the smallest temperature scales. This requires a thorough explanation given the fact that the low-temperature flow is intuitively expected to depend primarily on the gap region, where the metallic electrode induces constant and *ph*-symmetric TDOS. The same behavior was already observed in Ref. [50] for the SC-AIM+M case and was clearly linked to the underlying $\Gamma_M = 0$ version of the problem (SC-AIM). A detailed analysis of this issue is given at the end of this section.

The splittings induced by *ph*-asymmetry result in a diminishing difference between the ground-state singlet and the first excited doublet in the high-temperature flow, as shown in Fig. 11(e). Such behavior is a typical precursor for the singlet-doublet QPTs for $\Gamma_M = 0$. Note that such $E_n$ splittings had been noticed already for SC-AIM; see Fig. 2 in Ref. [76].
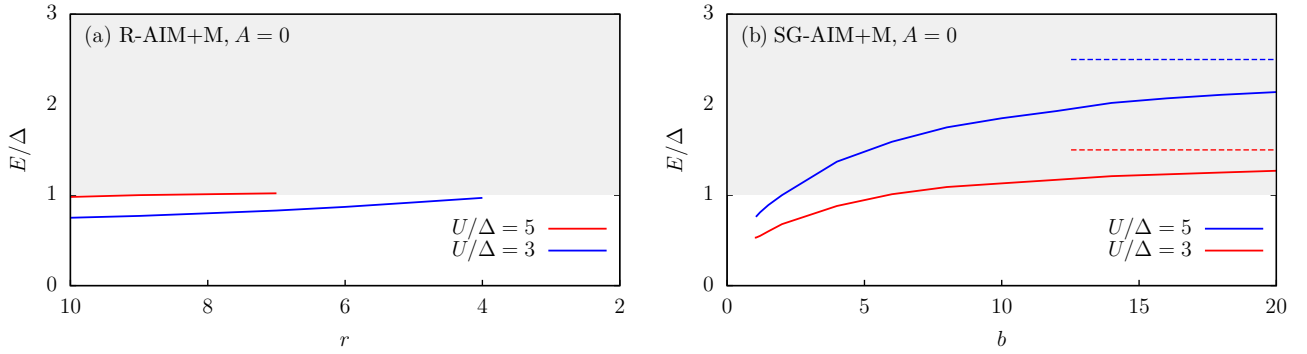
FIG. 12. (a) Position of the innermost peaks for R-AIM with $A = 0$ at two values of $U/\Delta$. (b) Position of the innermost peaks for SG-AIM with $A = 0$ at two values of $U/\Delta$.

However, the choice of parameters in the cited work obscured this observation. Yet, this is actually a consequence of fixing $\varphi = 0$ and selecting only the extreme cases with $\Delta \gg T_K$ and $\Delta \ll T_K$, where $T_K$ is the Kondo temperature. For $\Delta \approx T_K$, which was not addressed in the cited work, the splitting of $E_n$ values, which points towards the correspondence to AIM with QD out-of-half-filling, would be clearly visible.

### 5. Escape of broadened in-gap peaks into the continuum

SG-AIM and R-AIM have a continuous TDOS profile, and leakage of in-gap peaks into the continuous supragap spectrum might be expected. However, broadened in-gap peaks observed outside of the gap region cannot be strictly bound for the $\Gamma_M = 0$ counterpart of SG-AIM+M or R-AIM+M. On the other hand, G-AIM is defined to possess a finite discontinuity that is expected to provide a sufficient barrier toward the leakage. In this respect, the AGNR-AIM and the SC-AIM case after the transformation $\mathbb{T}$ both possess continuous TDOS features requiring a brief analysis. We stress that for any $\varphi \neq 0$, BCS-like divergences appear at the gap edges $\omega = \pm\Delta$. However, at $\varphi = 0$ the divergence at $\omega = \Delta$ vanishes and the profile becomes proportional to $|\omega|/\sqrt{\omega - \Delta}$ for $\omega > \Delta$, which is similar to the R-AIM profile. Nevertheless, no leakage of the inner in-gap state was reported here. This is probably a consequence of having yet another BCS-like divergence at $\omega = -\Delta$. We therefore focus on continuous TDOS cases of R-AIM and SG-AIM here.

First, let us analyze the $A = 0$ R-AIM case with its in-gap peak positions shown in Fig. 12(a). Here, the shaded region shows the supragap portion of the spectra, while below $E/\Delta < 1$ the broadened in-gap peaks are observed (the Kondo anomaly at $\omega = 0$ is omitted). Negative frequency regions are symmetric to the region shown in Fig. 12(a). Two values of $U/\Delta$ are used in order to demonstrate the expelling of broadened in-gap peaks (if present in the gap) to the gap edges with enhanced $U$. For R-AIM+M with $r = 10$ we observe a well-separated broadened in-gap state at $\omega/\Delta \approx 0.8$ for $U/\Delta = 3$. However, already at $U/\Delta = 5$ it becomes hardly distinguishable with the supragap part of the spectral function as it is expelled onto the gap edge $\omega/\Delta = 1$.

For R-AIM with $4 \leqslant r \leqslant 10$ it appears that an in-gap peak might be present for $U/\Delta = 3$ and lie in the vicinity of the gap edge. For $r \lesssim 4$ no features could be reliably identified

in supra- as well as subgap parts of the spectral functions for $U/\Delta = 3$. For $U/\Delta = 5$ the situation is analogous but is observed already at $r \approx 4$, and there are two reasonable ways to interpret such findings. The first is that the in-gap states for R-AIM do exist for a given threshold value of $r^*$ until they reach the gap edges. The excited states with exactly the same quantum states as before might exist also for $r > r^*$ but obtain resonant character as they move into the continuum. The second possibility is that they are not present at all, which would break the analogy to the SC-AIM here. Our present approach cannot give a conclusive answer as to which interpretation is correct. Nevertheless, we stress that even if it is the latter one, all remaining analogies with AGNR-AIM+M and SC-AIM+M still hold true. These include the presence of subgap Kondo peaks and traces of Kondo peaks in the supragap spectral function.

In SG-AIM+M systems the behavior becomes even more complex, as shown in Fig. 12(b). Setting first $b = 1$ at a given $U$ we completely recover the G-AIM+M case and its corresponding broadened in-gap peaks. Increasing then $U$ at fixed remaining model parameters shifts the in-gap peak against the gap edge $\omega/\Delta = 1$, which is a behavior analogous to that of AGNR-AIM or SC-AIM (where additional symmetrizations need to be considered). Additionally increasing $b$ makes the discontinuity of G-AIM+M smoother, which can also be understood as effective broadening of the gap region. Shifting of the in-gap states toward the gap edges is then an expected result. However, unlike in R-AIM+M systems, once the broadened in-gap peaks reach the smooth gap edge they do not vanish, and we may observe their transition into the supragap region. Since at $\Gamma_M = 0$ there is nonzero TDOS, in this region they cannot have bound character and are thus part of the continuous spectrum. Nevertheless, this behavior can still be attributed to the effective expansion of the gap region due to $b$.

The positions of the peaks approach approximately $\pm U/2$, which correspond to the positions of Hubbard peaks. It is thus obvious that by increasing the smoothness of the gap, their properties trivialize to those of ordinary Hubbard peaks. Incorporating $ph$-asymmetry into the TDOS will then force their movement towards Fermi energy. In such a case, it is difficult to make any conclusions about the correspondence to AGNR-AIM or SC-AIM cases. Consequently, it would be highly speculative to confirm or exclude the presence of

singlet-doublet transitions or any other QPTs. We stress that the escape into the continuum is also accompanied by weak-ening of reentrant behavior described in Sec. III, which only underlines the importance of careful RG analysis.

[1] L. Kouwenhoven and L. Glazman, Phys. World **14**, 33 (2001).

[2] N Agraït, A. L. Yeyati, and J. M. van Ruitenbeek, Phys. Rep. **377**, 81 (2003).

[3] S. De Franceschi, L. Kouwenhoven, C. Schönenberger, and W. Wernsdorfer, Nat. Nanotechnol. **5**, 703 (2010).

[4] F. Evers, R. Korytár, S. Tewari, and J. M. van Ruitenbeek, Rev. Mod. Phys. **92**, 035001 (2020).

[5] M. Žonda, O. Stetsovych, R. Korytár, M. Ternes, R. Temirov, A. Raccanelli, F. S. Tautz, P. Jelínek, T. Novotný, and M. Švec, J. Phys. Chem. Lett. **12**, 6320 (2021).

[6] A. C. Hewson, *The Kondo Problem to Heavy Fermions*, Cambridge Studies in Magnetism (Cambridge University Press, Cambridge, 1993).

[7] W. Chang, V. E. Manucharyan, T. S. Jespersen, J. Nygård, and C. M. Marcus, Phys. Rev. Lett. **110**, 217005 (2013).

[8] J.-D. Pillet, C. H. L. Quay, P. Morfin, C. Bena, A. L. Yeyati, and P. Joyez, Nat. Phys. **6**, 965 (2010).

[9] J. D. Pillet, P. Joyez, R. Žitko, and M. F. Goffman, Phys. Rev. B **88**, 045101 (2013).

[10] R. Delagrange, D. J. Luitz, R. Weil, A. Kasumov, V. Meden, H. Bouchiat, and R. Deblock, Phys. Rev. B **91**, 241401(R) (2015).

[11] R. Delagrange, R. Weil, A. Kasumov, M. Ferrier, H. Bouchiat, and R. Deblock, Phys. Rev. B **93**, 195437 (2016).

[12] T. Yoshioka and Y. Ohashi, J. Phys. Soc. Jpn. **69**, 1812 (2000).

[13] Y. Tanaka, A. Oguri, and A. C. Hewson, New J. Phys. **9**, 115 (2007).

[14] A. Kadlecová, M. Žonda, and T. Novotný, Phys. Rev. B **95**, 195114 (2017).

[15] A. Kadlecová, M. Žonda, V. Pokorný, and T. Novotný, Phys. Rev. Appl. **11**, 044094 (2019).

[16] A. Martín-Rodero and A. Levy Yeyati, Adv. Phys. **60**, 899 (2011).

[17] V. Meden, J. Phys.: Condens. Matter **31**, 163001 (2019).

[18] D. J. Luitz, F. F. Assaad, T. Novotný, C. Karrasch, and V. Meden, Phys. Rev. Lett. **108**, 227001 (2012).

[19] A. V. Rozhkov and D. P. Arovas, Phys. Rev. Lett. **82**, 2788 (1999).

[20] F. Siano and R. Egger, Phys. Rev. Lett. **93**, 047002 (2004).

[21] T. Novotný, A. Rossini, and K. Flensberg, Phys. Rev. B **72**, 224502 (2005).

[22] C. Karrasch, A. Oguri, and V. Meden, Phys. Rev. B **77**, 024517 (2008).

[23] E. Prada, P. San-Jose, M. W. A. de Moor, A. Geresdi, E. J. H. Lee, J. Klinovaja, D. Loss, J. Nygård, R. Aguado, and L. P. Kouwenhoven, Nat. Rev. Phys. **2**, 575 (2020).

[24] P. W. Anderson, Phys. Rev. **124**, 41 (1961).

[25] W. Metzner, M. Salmhofer, C. Honerkamp, V. Meden, and K. Schönhammer, Rev. Mod. Phys. **84**, 299 (2012).

[26] P. Kopietz, L. Bartosch, and F. Schütz, *Introduction to the Functional Renormalization Group*, Lecture Notes in Physics (Springer-Verlag, Berlin, 2010).

[27] S. Streib, A. Isidori, and P. Kopietz, Phys. Rev. B **87**, 201107(R) (2013).

[28] K. Edwards, A. C. Hewson, and V. Pandis, Phys. Rev. B **87**, 165128 (2013).

[29] S. Andergassen, T. Enss, C. Karrasch, and V. Meden, in *NATO Science for Peace and Security Series B: Physics and Biophysics* (Springer, The Netherlands, 2008), pp. 1–17.

[30] V. Janiš and P. Augustinský, Phys. Rev. B **75**, 165108 (2007).

[31] V. Janiš, P. Zalom, V. Pokorný, and A. Klíč, Phys. Rev. B **100**, 195114 (2019).

[32] E. Gull, A. J. Millis, A. I. Lichtenstein, A. N. Rubtsov, M. Troyer, and P. Werner, Rev. Mod. Phys. **83**, 349 (2011).

[33] J. E. Gubernatis, *Quantum Monte Carlo Methods: Algorithms for Lattice Models* (Cambridge University Press, New York, 2016).

[34] K. G. Wilson, Rev. Mod. Phys. **47**, 773 (1975).

[35] H. R. Krishna-murthy, J. W. Wilkins, and K. G. Wilson, Phys. Rev. B **21**, 1003 (1980).

[36] H. R. Krishna-murthy, J. W. Wilkins, and K. G. Wilson, Phys. Rev. B **21**, 1044 (1980).

[37] R. Bulla, T. A. Costi, and T. Pruschke, Rev. Mod. Phys. **80**, 395 (2008).

[38] T. Meng, S. Florens, and P. Simon, Phys. Rev. B **79**, 224521 (2009).

[39] J. Bauer, A. Oguri, and A. C. Hewson, J. Phys.: Condens. Matter **19**, 486211 (2007).

[40] Y. Tanaka, N. Kawakami, and A. Oguri, J. Phys. Soc. Jpn. **76**, 074701 (2007).

[41] R. Žitko, Phys. Rev. B **93**, 195125 (2016).

[42] M. Žonda, V. Pokorný, V. Janiš, and T. Novotný, Phys. Rev. B **93**, 024523 (2016).

[43] D. Goldhaber-Gordon, J. Göres, M. A. Kastner, H. Shtrikman, D. Mahalu, and U. Meirav, Phys. Rev. Lett. **81**, 5225 (1998).

[44] M. R. Galpin and D. E. Logan, Phys. Rev. B **77**, 195108 (2008).

[45] M. R. Galpin and D. E. Logan, Eur. Phys. J. B **62**, 129 (2008).

[46] K. Takegahara, Y. Shimizu, and O. Sakai, J. Phys. Soc. Jpn. **61**, 3443 (1992).

[47] C. P. Moca and A. Roman, Phys. Rev. B **81**, 235106 (2010).

[48] K. Chen and C. Jayaprakash, Phys. Rev. B **57**, 5225 (1998).

[49] J. Pinto and H. Frota, J. Magn. Magn. Mater. **379**, 217 (2015).

[50] P. Zalom, V. Pokorný, and T. Novotný, Phys. Rev. B **103**, 035419 (2021).

[51] G. Diniz, G. S. Diniz, G. B. Martins, and E. Vernek, Phys. Rev. B **101**, 125115 (2020).

[52] P. Zalom and T. Novotný, Phys. Rev. B **104**, 035437 (2021).

[53] E. N. Economou, *Green's Functions in Quantum Physics* (Springer, Berlin, 2006).

[54] K. Satori, H. Shiba, O. Sakai, and Y. Shimizu, J. Phys. Soc. Jpn. **61**, 3239 (1992).

[55] H. Xiao, J. Tahir-Kheli, and W. A. Goddard, J. Phys. Chem. Lett. **2**, 212 (2011).

[56] J. M. Crowley, J. Tahir-Kheli, and W. A. Goddard III, J. Phys. Chem. Lett. **7**, 1198 (2016).

[57] W. H. Appelt, A. Droghetti, L. Chioncel, M. M. Radonjió, E. Muñoz, S. Kirchner, D. Vollhardt, and I. Rungger, Nanoscale **10**, 17738 (2018).

[58] I. S. Beloborodov, A. V. Lopatin, G. Schwiete, and V. M. Vinokur, Phys. Rev. B **70**, 073404 (2004).

[59] Y.-C. Sun, S.-S. Yeh, and J.-J. Lin, Phys. Rev. B **82**, 054203 (2010).

[60] More rigorously, Kondo temperature should to be extracted from well-converged spectral functions or magnetic susceptibility.

[61] I. Affleck and A. W. W. Ludwig, Phys. Rev. B **48**, 7297 (1993).

[62] D. Friedan and A. Konechny, Phys. Rev. Lett. **93**, 030402 (2004).

[63] We stress that Hubbard peaks due to bare $\Gamma_S$ and $U$ interfere with the high-temperature traces of the Kondo peak, a situation analogous to that of Figs. 2(e) and 2(f) in Ref. [52].

[64] Y. Li, A. T. Ngo, A. DiLullo, K. Z. Latt, H. Kersell, B. Fisher, P. Zapol, S. E. Ulloa, and S.-W. Hla, Nat. Commun. **8**, 946 (2017).

[65] R. Temirov, A. Lassise, F. B. Anders, and F. S. Tautz, Nanotechnology **19**, 065401 (2008).

[66] J. C. Oberg, M. R. Calvo, F. Delgado, M. Moro-Lagares, D. Serrate, D. Jacob, J. Fernández-Rossier, and C. F. Hirjibehedin, Nat. Nanotechnol. **9**, 64 (2014).

[67] R. Maurand, T. Meng, E. Bonet, S. Florens, L. Marty, and W. Wernsdorfer, Phys. Rev. X **2**, 011009 (2012).

[68] G. L. Hansen, J. L. Schmit, and T. N. Casselman, J. Appl. Phys. **53**, 7099 (1982).

[69] J. C. Estrada Saldaña, A. Vekris, V. Sosnovtseva, T. Kanne, P. Krogstrup, K. Grove-Rasmussen, and J. Nygård, Commun. Phys. **3**, 125 (2020).

[70] R. Bulla, J. Keller, and T. Pruschke, Z. Phys. B **94**, 195 (1994).

[71] R. Zitko, NRG Ljubljana (Zenodo, 2021), doi: 10.5281/zenodo.4841076.

[72] R. Žitko and T. Pruschke, Phys. Rev. B **79**, 085106 (2009).

[73] R. Bulla, A. C. Hewson, and T. Pruschke, J. Phys.: Condens. Matter **10**, 8365 (1998).

[74] Note that in Fig. 9(a) we present the flow for the even NRG iterations, which have the advantage of correctly ascribing the quantum numbers to the ground state. Odd NRG iterations carry the same information about the effective behavior, but the $E_n$ values, their quantum numbers, and multiplicities completely differ compared to the picture with even iterations. In the end, the choice is arbitrary and just a matter of convenience.

[75] For $\delta < 0$, the doubly occupied QD is left.

[76] T. Hecht, A. Weichselbaum, J. von Delft, and R. Bulla, J. Phys.: Condens. Matter **20**, 275213 (2008).